SKI Report 2005:16

Research

Assessment of Core Failure Limits for Light Water Reactor Fuel under Reactivity Initiated Accidents

Lars Olof Jernkvist
Ali R. Massih

December 2004

ISSN 1104–1374
ISRN SKI-R-05/16-SE

SKI Perspective

Background and purpose of the project

Over the last 10 years the behaviour of nuclear fuel during reactivity initiated accidents has been studied to investigate the failure threshold as a function of burnup. Experimental programmes performed in the CABRI test reactor (France) and in the Nuclear Safety Research Reactor (Japan) have indicated that cladding failure and fuel dispersion of high burnup fuel may occur at enthalpy values lower than previously estimated.

At the beginning of 1995 SKI issued fuel and cladding failure limits based on available test data. It was envisaged at that time that the failure limits should be re-evaluated when more information was available. Since then SKI has joined the OECD-IRSN CABRI water loop project at the end of 2000. The purpose was to gain information on the failure threshold for nuclear fuel cladding as a function of burnup, especially for modern cladding materials and during prototypical conditions.

In 2003 SKI initiated a study, in cooperation with the Swedish nuclear utilities, to recommend more relevant fuel and cladding failure limits for reactivity initiated accidents.

The work presented in this report is the fourth part of the study. In the report core failure thresholds are calculated for high burnup light water reactor fuel by use of best-estimate computational methods.

In the first part a strain-based failure criterion was formulated based on mechanical tests and compared with experimental tests and other failure criterion. This is reported in SKI report 2004:32. The second part, which consists of fuel failure thresholds calculated by use of best-estimate computational methods, is reported in SKI report 2004:33. The third part is a sensitivity study which is reported in SKI report 2004:34.

Results

This project has contributed to the research goal of giving a basis for SKIs supervision by means of evaluating and modelling the nuclear fuel cladding failure threshold during a design base accident. The project has also contributed to the research goal to develop the competence about licensing of fuel at high burnup, which is an important safety issue.

Projekt information

SKI Project Manager: Jan in de Betou
Project Identification Number: 200306004

SKI Report 2005:16

Research

Assessment of Core Failure Limits for Light Water Reactor Fuel under Reactivity Initiated Accidents

Lars Olof Jernkvist
Ali R. Massih

Quantum Technologies AB
Uppsala Science Park
SE-751 83 Uppsala
Sweden

December 2004

List of contents

List of appendices

Summary

Core failure limits for high-burnup light water reactor UO_2 fuel rods, subjected to postulated reactivity initiated accidents (RIAs), are here assessed by use of best-estimate computational methods. The considered RIAs are the hot zero power rod ejection accident (HZP REA) in pressurized water reactors and the cold zero power control rod drop accident (CZP CRDA) in boiling water reactors. Burnup dependent core failure limits for these events are established by calculating the fuel radial average enthalpy connected with incipient fuel pellet melting for fuel burnups in the range of 30 to 70 $MWd(kgU)^{-1}$. The postulated HZP REA and CZP CRDA result in lower enthalpies for pellet melting than RIAs that take place at rated power. Consequently, the enthalpy thresholds presented here are lower bounds to RIAs at rated power.

The calculations are performed with best-estimate models, which are applied in the FRAPCON-3.2 and SCANAIR-3.2 computer codes. Based on the results of three-dimensional core kinetics analyses, the considered power transients are simulated by a Gaussian pulse shape, with a fixed width of either 25 ms (REA) or 45 ms (CRDA). Notwithstanding the differences in postulated accident scenarios between the REA and the CRDA, the calculated core failure limits for these two events are similar. The calculated enthalpy thresholds for fuel pellet melting decrease gradually with fuel burnup, from approximately 960 $J(gUO_2)^{-1}$ at 30 $MWd(kgU)^{-1}$ to 810 $J(gUO_2)^{-1}$ at 70 $MWd(kgU)^{-1}$. The decline is due to depression of the UO_2 melting temperature with increasing burnup, in combination with burnup related changes to the radial power distribution within the fuel pellets.

The presented fuel enthalpy thresholds for incipient UO_2 melting provide best-estimate core failure limits for low- and intermediate-burnup fuel. However, pulse reactor tests on high-burnup fuel rods indicate that the accumulation of gaseous fission products within the pellets may lead to fuel dispersal into the coolant at significantly lower enthalpies than those required for melting, when the fuel burnup exceeds approximately 40 $MWd(kgU)^{-1}$. This issue is investigated by reviewing all high-burnup UO_2 fuel rods that have failed in RIA simulation tests in the Japanese Nuclear Safety Research Reactor and the French CABRI pulse reactor to date. Data from thirteen failed rods, with burnups between 44 and 64 $MWd(kgU)^{-1}$, indicate that clad tube failure does not necessarily lead to fuel pellet dispersal. In fact, the data suggest that a peak fuel radial average enthalpy of at least 500 $J(gUO_2)^{-1}$ is required to expel a significant part (>10 %) of the fuel inventory into the coolant. However, this empirical enthalpy threshold for fuel dispersal from high-burnup fuel rods cannot be directly applied to light water reactors, since the power pulses and/or the cooling conditions used in the pulse tests differ notably from those expected in LWRs under RIA.

Sammanfattning

I denna rapport används realistiska beräkningsmodeller för att fastställa härdskadegränser gällande högutbrända urandioxidbränslestavar under postulerade reaktivitetsinitierade olyckor (RIA) i lättvattenreaktorer. Två skilda reaktivitetsolyckor beaktas: styrstavsutskjutning vid nolleffekt och varm härd (HZP REA) i tryckvattenreaktorer, samt fallande styrstav vid nolleffekt och kall härd (CZP CRDA) i kokvattenreaktorer. För dessa två fall bestäms utbränningsberoende härdskadegränser genom att beräkna den bränsleentalpi som ger upphov till begynnande smältning av bränslekutsarna. Detta görs för utbränningar från 30 till 70 MWd(kgU)$^{-1}$. De postulerade reaktivitetsolyckorna vid nolleffekt resulterar i lägre entalpigränser för smältning av bränslekutsarna än motsvarande olyckor vid högre reaktoreffekt, vilket medför att de entalpigränser som presenteras här utgör undre gränser för RIA vid hög reaktoreffekt.

För beräkningarna används "best-estimate"-modeller i beräkningsprogrammen FRAPCON-3.2 och SCANAIR-3.2. Baserat på resultat av tredimensionella härdkinetikanalyser ansätts en Gaussformad effektpuls med en pulsvidd om antingen 25 ms (REA) eller 45 ms (CRDA) för att simulera reaktivitetsolyckan. Trots skillnaderna i postulerade förlopp för de två beaktade olyckorna, så är de beräknade härdskadegränserna likartade för de två fallen. De beräknade tröskelentalpierna för bränslesmältning faller gradvis med ökande utbränning, från omkring 960 J(gUO_2)$^{-1}$ vid 30 MWd(kgU)$^{-1}$ till 810 J(gUO_2)$^{-1}$ vid 70 MWd(kgU)$^{-1}$. Denna minskning beror på att urandioxidens smältpunkt sjunker med ökande utbränning, samtidigt som den radiella effektfördelningen i kutsen förändras.

De presenterade entalpigränserna för begynnande smältning av urandioxiden utgör realistiska härdskadegränser för bränsle med måttlig utbränning. Dock visar pulsreaktorförsök utförda på högutbrända bränslestavar att ansamlingen av gasformiga fissionsprodukter i bränslekutsarna kan leda till utslungande av bränsle i kylvattnet vid betydligt lägre entalpinivåer, då utbränningen överstiger ungefär 40 MWd(kgU)$^{-1}$. Detta fenomen undersöks genom att utvärdera samtliga högutbrända bränslestavar med urandioxidkutsar, som till dags dato har havererat under simulerade RIA i pulsreaktorerna NSRR, Japan, och CABRI, Frankrike. Data från tretton havererade stavar, med utbränningar mellan 44 och 64 MWd(kgU)$^{-1}$, visar att kapslingsskador ej nödvändigtvis leder till spridning av bränsle i kylvattnet. Pulsreaktorproven antyder att en bränsleentalpi (radiellt medelvärde för kutsen) överstigande 500 J(gUO_2)$^{-1}$ krävs för utspridning av en betydande andel (>10 %) av bränsleinventariet i kylvattnet. Denna empiriska entalpigräns för bränsleutspridning från högutbrända bränslestavar kan emellertid ej direkt överföras till lättvattenreaktorer, då de effektpulser och kylförhållanden som används vid pulsreaktorproven skiljer sig avsevärt från förväntade förhållanden under reaktivitetsolyckor i lättvattenreaktorer.

1 Introduction

Reactivity initiated accidents (RIAs) are important design basis events in light water reactors (LWRs), which involve inadvertent removal of a control element from the reactor core. In pressurized water reactors (PWRs), the accident scenario of primary concern is the control rod ejection accident (REA). The REA is caused by mechanical failure of a control rod mechanism housing, such that the coolant pressure ejects a control rod assembly completely out of the core (Glasstone & Sesonske, 1991). In boiling water reactors (BWRs), the most severe scenario for RIA is the control rod drop accident (CRDA). The initiating event for the CRDA is the separation of a control rod blade from its drive mechanism. The separation takes place when the blade is inserted in the core, and the detached blade remains stuck in this position until it suddenly becomes loose and drops out of the core in a free fall.

Both the PWR REA and the BWR CRDA result in a rapid power excursion in fuel assemblies close to the failed control element. If the reactivity worth of the ejected control element is high, the rapid energy deposition in adjacent fuel assemblies may be sufficient to cause fuel failure. In order to assure long-term core coolability and to prevent mechanical damage to the reactor pressure vessel from pressure pulses in the coolant during RIA, licensing limits for the fuel pellet enthalpy are prescribed. These limits are intended to ensure core coolability and pressure vessel integrity by precluding fragmentation of the fuel and generation of destructive pressure pulses through violent fuel-coolant interaction. The current core failure limit applied in Sweden for reactivity initiated accidents is presented in appendix A. This limit is based on the results of RIA simulation test, performed in pulse reactors. The power pulses and cooling conditions in these experiment reactors are unfortunately not typical for those expected in commercial light water reactors under an RIA, which makes it difficult to establish failure limits by direct rendition of test data.

The work presented in this report is aimed at establishing core failure limits for high-burnup light water reactor fuel rods under RIA by use of best-estimate computer analyses. Core failure limits are calculated for two hypothetical reactivity initiated accidents in light water reactors: the hot zero power (HZP) rod ejection accident in pressurized water reactors, and the cold zero power (CZP) control rod drop accident in boiling water reactors. The failure limits are established by calculating the fuel enthalpy connected with incipient fuel pellet melting for fuel burnups in the range of 30 to 70 $MWd(kgU)^{-1}$. The calculations are performed with best-estimate computational models, but penalizing assumptions are made in input to the analyses, in order to account for uncertainties associated with high-burnup fuel behaviour under fast power transients.

The organization of the report is as follows:

The background to the existing core failure limit for RIA is presented in section 2, where also a brief introduction to the physical phenomena related to fragmentation and dispersal of nuclear fuel under RIA is given.

The computational models and methods applied in analyses are described in section 3, together with the assumptions made about fuel rod design, steady-state base irradiation conditions and the postulated reactivity initiated accidents.

Section 4 contains the results of the performed analyses. Calculated burnup dependent fuel rod conditions prior to RIA, such as clad corrosion and pellet-clad gap conditions, are first presented in section 4.1. These calculated conditions serve as input to the analyses of the actual RIA, the results of which are compiled in section 4.2. Here, the calculated core failure limits are presented, together with data on the fuel temperature distribution at the time of incipient melting.

The calculated core failure limits are discussed and evaluated in section 5 of the report, where comparisons are made with the current core failure limit for RIA in Sweden. A comparison is also made with a recent study by the Electric Power Research Institute in the USA, in which a core failure limit for high-burnup pressurized water reactor fuel has been calculated with methods similar to those used in our study. Finally, we also summarize the experience gained from pulse reactor tests, concerning dispersal of solid fuel particles from failed high-burnup fuel rods.

2 Background to core failure limits for RIA

2.1 Early pulse reactor tests on fresh and low-burnup fuel

In the late seventies, the United States Nuclear Regulatory Commission (US NRC) established two acceptance criteria for reactivity initiated accidents, based on results from RIA simulation tests performed on fresh and low-burnup fuel rods in pulse reactors (MacDonald, et al., 1980). These criteria, the details of which are given in (RG-1.77, 1974) and (NUREG-0800, 1981), have been used worldwide in their original or slightly modified forms:

Firstly, a fuel rod failure threshold was defined, stating that clad failure should be assumed in fuel rods that experience radially averaged fuel enthalpies above 170 $cal(gUO_2)^{-1}$ (712 $J(gUO_2)^{-1}$) at any axial location. This failure threshold is used in evaluations of radiological consequences of escaped fission products from failed rods, and it is not a definite operating limit. Hence, fuel enthalpies above this threshold are allowed in some of the fuel rods during an RIA. The failure threshold is applicable to RIA events initiated from zero or low power, i.e. in practice to BWR RIA at CZP conditions. For RIAs taking place at rated power conditions, fuel rods that experience dry-out (BWR) or departure from nucleate boiling (PWR) should be assumed to fail.

Secondly, a core failure limit was defined, stating that the radial average fuel enthalpy may not exceed 280 $cal(gUO_2)^{-1}$ (1172 $J(gUO_2)^{-1}$) at any axial location in any fuel rod. Fuel enthalpies above this limit were experimentally found to cause UO_2 fuel melting, fragmentation of the cladding and violent expulsion of the molten fuel into the coolant water. This failure process is primarily caused by volumetric expansion of UO_2, when the material changes from solid to liquid phase. The expulsion of molten fuel led to energetic fuel-coolant interaction, involving fragmentation of the fuel pellets into fine particles and generation of pressure pulses in the coolant. Consequently, the core failure limit was set to 280 $cal(gUO_2)^{-1}$ in order to ensure core coolability and reactor pressure vessel integrity by precluding the expulsion of molten fuel particles into the coolant.

Unfortunately, this core failure limit was actually set in error: As noted by MacDonald et al. (1980), the US NRC mistakenly expressed the limit in terms of radial average peak fuel enthalpy, whereas the supporting experimental data were reported in terms of radial average total energy deposition. The radial average peak fuel enthalpy is less than the associated radial average total energy deposition, due to fuel-to-coolant heat transfer under the power transient, and also since a large fraction of the total energy is due to delayed fission. If this mistake is corrected, the core failure limit is reduced to 230 $cal(gUO_2)^{-1}$ (963 $J(gUO_2)^{-1}$). This is the value currently applied in Sweden as core failure limit for low- and intermediate-burnup fuel under reactivity initiated accidents; see appendix A. For high-burnup fuel, the current core failure limit applied in Sweden is significantly reduced from this value, based on observations made in more recent pulse reactor tests. This is further discussed in the sequel.

2.2 Recent pulse reactor tests on high-burnup fuel

RIA simulation tests carried out on high-burnup fuel rods in the French CABRI test reactor and the Japanese Nuclear Safety Research Reactor (NSRR) during the last decade have shown that a potential exists for dispersal of non-molten fuel fragments at fuel radial average enthalpies well below 800 $J(gUO_2)^{-1}$ (Sugiyama & Fuketa, 2000). More precisely, dispersal of non-molten fuel has to date been observed in nine pulse reactor tests on light water reactor fuel rods, ranging in burnup from 44 to 64 $MWd(kgU)^{-1}$. These rods were subjected to power pulses with peak radial average fuel enthalpies between 306 and 657 $J(gUO_2)^{-1}$ in the CABRI reactor and the NSRR. A compilation of data on all pre-irradiated fuel rods that have failed in RIA simulation tests up to December 2004 is given in appendix B.

In summary, the tests reviewed in appendix B indicate that mechanisms other than fuel melting may lead to dispersal of fragmented fuel into the coolant, when the fuel burnup exceeds approximately 40 $MWd(kgU)^{-1}$. This finding raises concerns about the core coolability, since the dispersal of non-molten fuel particles may lead to loss of coolable fuel geometry, generation of detrimental pressure pulses in the coolant, and possibly also to flow blockage in some fuel assemblies. These potential consequences are related to the amount, thermal energy and particle size of the fuel material dispersed into the coolant.

2.3 Mechanisms for dispersal of high-burnup fuel

In ceramographic examinations of UO_2 fuel that has undergone RIA simulation tests in pulse reactors, it is usually found that the outer part of the fuel pellet is severely fragmented (Lespiaux et al., 1997) and (Fuketa et al., 2000). Typically, a large number of radial cracks are seen at the pellet surface, and these cracks extend a few millimetres towards the pellet centre. These fairly long cracks are probably caused by tensile hoop stresses during cool-down of the pellet periphery, i.e. the cracks nucleate fairly late in the transient. In some cases, circumferential macroscopic cracks are also found at the boundary between the re-structured rim zone (see below) and the subjacent part of the pellet. These cracks are most likely caused by tensile radial stresses during the early heat-up phase.

The radial and circumferential cracks described above create fairly large fuel fragments, which are not so easily expelled through cladding cracks in a failed fuel rod. However, in high-burnup fuel, much finer fragments are usually observed along the periphery of the pellet. These fragments are believed to result from grain decohesion, caused by overpressurization of gas-filled pores and intergranular gas bubbles under rapid rise in temperature (Lemoine, 1997). The resulting fragments are very small, typically about 50 µm, and can therefore be more easily expelled through cladding cracks in a failed fuel rod (Lespiaux et al., 1997) and (Fuketa et al., 1997). Hence, post-failure fuel dispersal is promoted by this fragmentation mechanism, which is typical of high-burnup fuel.

Of particular importance to the grain boundary decohesion is the formation of a typical high-burnup microstructure (rim zone) at the pellet periphery.

As a consequence of accumulated fission products, enhanced local burnup and fission rate in combination with low temperature, a restructuring of the fuel material takes place at the pellet peripheral rim in high-burnup fuel. Formation of this rim zone microstructure is characterized by a simultaneous reduction in grain size, increase in porosity and depletion of fission gas from the UO_2 matrix (Jernkvist & Massih, 2002). The rim zone microstructure, with its high density of grain boundaries and gas-filled pores, is therefore sensitive to fragmentation by grain boundary decohesion under RIA. The rim zone formation starts at a local burnup[1] of 60-70 MWd(kgU)$^{-1}$ by subdivision of grains at the fuel pellet outer surface, and at pores and bubbles close to the surface. The progression of the restructuring process, and the inward propagation of the rim zone towards the pellet centre, is controlled by the radial distributions of both fissile material and temperature. In commercial LWR fuel, the radial width of the rim zone is usually less than 200 µm, which means that the rim zone constitutes less than 10 % of the total fuel volume.

The current core failure limit for reactivity initiated accidents in Sweden is set with consideration of the increased potential for dispersal of non-molten fuel fragments from failed high-burnup fuel rods. As shown in appendix A, the core failure limit is reduced to 100 cal(gUO_2)$^{-1}$ at a fuel burnup of 45.4 MWd(kgU)$^{-1}$, and beyond this burnup, the core failure limit coincides with the fuel rod failure threshold (SKI, 1995). Hence, beyond 45.4 MWd(kgU)$^{-1}$, the current core failure limit is based on the assumption that a significant part of the fuel inventory of the rod is dispersed into the coolant following clad tube failure.

2.4 Fuel-coolant interaction

As mentioned in section 2.1, the core failure limit is intended to ensure long-term core coolability and to preclude damage to the reactor pressure vessel and internal core structures. Scenarios for loss of long-term core coolability after an RIA involve loss of coolable fuel geometry, for instance by melting, fragmentation or ballooning of the fuel rods. A coolable fuel geometry may also be lost if large amounts of fuel pellet fragments are dispersed into the coolant under RIA. Firstly, the dispersed fuel particles themselves may block flow channels and impair long-term cooling, or simply pile up at the bottom of the core in a configuration not amenable to cooling. Secondly, the dispersed fuel particles interact thermally with the coolant. The fuel-coolant interaction (FCI) could generate pressure waves in the coolant, which may damage nearby fuel assemblies and possibly also other core structures and the reactor pressure vessel (Berthoud, 2000).

To the author's knowledge, attempts to study the process of multi-rod failure by generation of coolant pressure waves have been made in only one RIA simulation test. This test, known as RIA 1-4, was carried out on a 3×3 array of PWR fuel rods in the Power Burst Facility (PBF) at the Idaho National Laboratory in the late seventies (Cook & Martinson, 1984).

[1] Corresponds to a pellet radial average burnup of approximately 40-45 MWd(kgU)$^{-1}$ in commercial LWR fuel rods with typically 3 - 5% enrichment of ^{235}U.

The test rods were pre-irradiated to a burnup of 4-6 MWd(kgU)$^{-1}$, after which they were subjected to a 11 ms wide power pulse in the PBF, resulting in peak radial average fuel enthalpies in the range of 980 to 1160 J(gUO_2)$^{-1}$. All the rods failed by axial cracks, induced by pellet-clad mechanical interaction, and one of the rods also experienced partial melting of the clad tube. However, no fuel material was dispersed into the coolant and detrimental pressure waves were therefore not generated. Consequently, the test failed to demonstrate the propagation of fuel rod damage from a failed rod to its neighbours by fuel dispersal and pressure wave generation. Further tests are therefore warranted to elucidate this hypothetical damage mechanism.

By convention, the degree of fuel-coolant interaction is quantified with the energy conversion ratio, which is the ratio of the kinetic energy generated in the coolant to the thermal energy in the dispersed fuel. This ratio can be determined in pulse reactor tests, where the mechanical energy generated in the coolant is estimated by measuring the motion of the water column in the test rig, as it is raised by rapid expansion of steam bubbles around dispersed fuel fragments.

Energetic FCI, known as vapour explosions, may take place when molten fuel is dispersed into water. In vapour explosions, the timescale for heat transfer from the molten fuel to the coolant is shorter than the timescale for pressure relief. Therefore, the local surge in coolant pressure forms a shock wave, which propagates with a velocity greater than the characteristic speed of sound in the coolant ahead of the shock front (Berthoud, 2000). The key feature of a vapour explosion is that the shock wave propagation through the coolant drives the rapid fuel fragmentation and associated heat transfer to the coolant, on the analogy of shock heating in a chemical detonation. In practise, fuel-coolant interaction does not generally exhibit these shock wave characteristics. The fragmentation of dispersed fuel particles is not necessarily linked to shock wave propagation, and the rapid boiling phenomenon propagates slower than the speed of sound. Although the character of the FCI is not explosive in this case, a large amount of vapour may be produced and detrimental pressure transients generated.

An upper limit for the energy conversion ratio under FCI can be calculated from thermodynamics, by assuming ideal mixing and isentropic expansion of the fuel-coolant mixture (Corradini et al., 1988). The energy conversion ratio depends on the ratio between fuel and coolant volumes involved in the process, but for molten UO_2 fuel dispersed into water at typical PWR conditions, the ideal conversion ratio is greater than 10 % for a wide range of fuel-to-coolant volume ratios. Much lower values are generally obtained in experiments (Berthoud, 2000). In particular, early RIA simulation tests on fresh fuel have shown that energy conversion ratios may reach up to about 1 %, when molten fuel is dispersed into water (Tsuruta et al., 1985). More recent tests in the NSRR have shown that about the same energy conversion ratios are reached, when solid high-burnup fuel is dispersed into water (Sugiyama & Fuketa, 2000). This is a somewhat controversial result, since the energy transfer to the water is generally believed to be more efficient for molten than for solid fuel particles. This follows from the fact that molten fuel particles are more easily fragmented than solid particles, when dispersed into water. The conversion ratio is higher for fine particles, since the specific surface (surface to volume ratio) is larger.

However, the results of the recent NSRR tests can be understood from the fact that conversion ratios for both molten and solid fuel depend on the initial size of the dispersed particles. As discussed in the previous section, the solid fuel particles that are expelled from high-burnup fuel rods are typically about 50 µm in size (Nakamura et al., 2002a). This should be compared with molten low-burnup fuel particles, which are at least about an order of magnitude larger (Tsuruta et al., 1985). Considering these differences in dispersed particle size between molten low-burnup and solid high-burnup fuel, the energy conversion ratio for the dispersed particles seems to be comparable for low- and high-burnup fuel. Consequently, it seems possible to correlate the mechanical energy generated in the coolant solely to the amount and enthalpy of the dispersed fuel, without discriminating between low-burnup molten fuel and high-burnup solid material.

The energy conversion ratios discussed above have been measured in water at room temperature and atmospheric pressure. The results are thus applicable to RIA at cold zero power conditions in a BWR, but not necessarily to hot zero power conditions in a PWR. As further discussed in section 5.3, the interaction between dispersed fuel and water is affected by the coolant temperature and pressure.

Finally, it should be remarked that pressure waves can in fact be generated without fuel dispersal, by release of the plenum gas inventory from failed fuel rods. However, experiments have shown that mechanical energy deposition from leaking gas is moderate in comparison with that from thermal interaction between dispersed fuel and the coolant (Sugiyama & Fuketa, 2000).

3 Analyses

The computational procedures and input data applied in this work are almost identical to those used in a companion assessment of fuel rod failure thresholds for RIA by Jernkvist and Massih (2004). The major difference between the two studies is in the applied failure criteria.

3.1 Scope of analyses

The hypothetical reactivity initiated accidents considered in this report are the hot zero power rod ejection accident in pressurized water reactors and the cold zero power control rod drop accident in boiling water reactors. In both these scenarios, mechanical failure of a control rod drive mechanism leads to a prompt power excursion, which initiates from near zero power conditions and terminates by negative feedback from the fuel temperature rise (Doppler effect). The power pulse widths considered in analyses are 25 ms for the PWR HZP REA and 45 ms for the BWR CZP CRDA; see section 3.3.3 for further details on the assumptions made about the reactivity initiated accidents.

The thermo-mechanical response of typical PWR and BWR fuel rods to these transients is analysed, using best-estimate computational models. Best-estimate core failure limits for PWR HZP REA and BWR CZP CRDA, in terms of peak radial average fuel enthalpy that can be sustained under RIA without fuel pellet melting, are calculated for fuel burnups in the range of 30 to 70 MWd(kgU)$^{-1}$. The upper end of this interval corresponds to the highest burnups, for which the computer codes and models applied in analyses have been verified with experimental data (Lanning et al., 1997). The computational models and methods are described in section 3.2 below, and key input is defined in section 3.3. The applicability of the calculated failure limits is discussed in section 5.1, where also the limitations of the performed analyses are defined.

3.2 Computational models and methods

3.2.1 Computer codes

The fuel rod thermo-mechanical behaviour under RIA is analysed by use of the SCANAIR-3.2 computer code (Federici et al., 2000). Since SCANAIR lacks models for simulation of long-term steady-state irradiation, the SKI-version of the FRAPCON-3.2 steady-state fuel performance code is used to establish burnup dependent initial conditions to the transient analyses (Berna et al., 1997). This version of FRAPCON-3.2 is equipped with an interface to SCANAIR-3.2 (Jernkvist, 2002). Both SCANAIR and FRAPCON are best-estimate computational tools, and throughout the performed analyses, the computer codes are used with their default best-estimate models. For the purpose of our analyses, however, the model for UO_2 thermal conductivity in SCANAIR is slightly modified, and some specific models are also added to the codes. These modifications and extensions are described in section 3.2.3 below.

3.2.2 Computational procedure

The computer codes described above are used for determining burnup dependent core failure limits in terms of enthalpy thresholds for incipient fuel pellet melting under PWR HZP REA and BWR CZP CRDA. Both limits are determined by the same procedure, as illustrated in figure 3.1. First, a generic base irradiation history is simulated by FRAPCON-3.2 up to a desired fuel burnup, in order to generate burnup dependent fuel rod initial conditions needed for transient analysis with SCANAIR-3.2. With these initial conditions, SCANAIR is then used to analyse the fuel rod response to the reactivity initiated event, which is represented by a Gaussian power pulse with a fixed width of either 25 ms (PWR) or 45 ms (BWR). These pulse widths are selected based on the results of three-dimensional core kinetics analyses of RIA, as described in section 3.3.3. The pulse amplitude is taken as a free parameter, and SCANAIR is run in an iterative loop in order to determine the pulse amplitude at which incipient fuel pellet melting is predicted. Once this critical pulse amplitude is found, iterations are terminated and the corresponding threshold fuel enthalpy is recorded in a diagram with respect to fuel burnup. By repeating this FRAPCON-SCANAIR analysis procedure for about 10 burnup levels in the range of 30 to 70 MWd(kgU)$^{-1}$, a burnup dependent enthalpy limit for incipient fuel melting is determined. The failure limit is reported in terms of peak radial average enthalpy under the pulse, as a function of pellet radial average burnup at the axial position of the rod where melting is imminent.

The full-length fuel rod is modelled in all analyses with FRAPCON and SCANAIR. The same axial discretization, consisting of 10 equal-length axial segments, is used for both computer codes. In analyses with SCANAIR, the pellet melt criterion is applied to each of the 10 axial segments of the discretized fuel rod. However, pellet melting is predicted always to occur at the axial position of peak power, which is the 9th and 6th axial segment from the bottom of the rod for the PWR and BWR fuel rod, respectively.

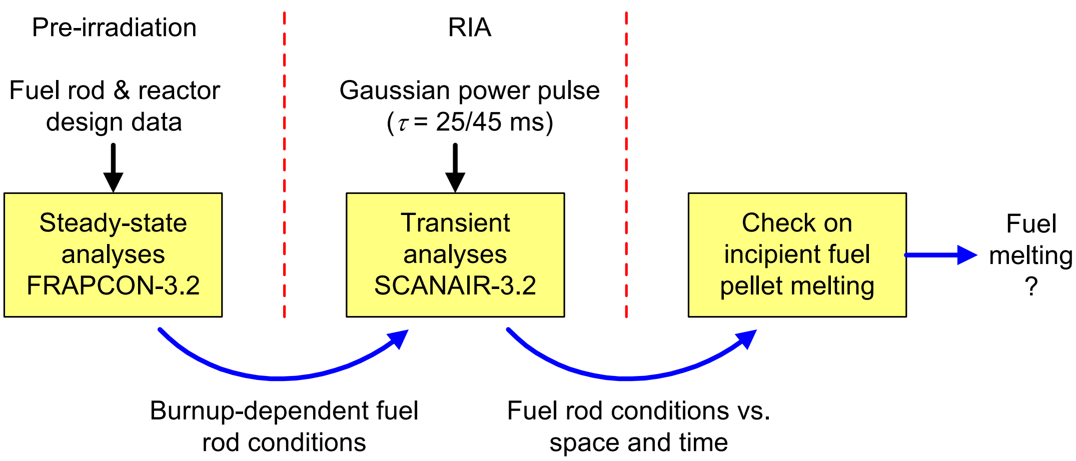

Figure 3.1: Computational procedure applied in analyses.

3.2.3 Specific models introduced for the present analyses

3.2.3.1 Fuel pellet high-burnup rim properties

The models for fission gas release and pellet gas-induced deformations applied in the SCANAIR-3.2 computer code require detailed information about the burnup dependent variation in material microstructure along the fuel pellet radius. Of particular interest is the formation of a characteristic high-burnup microstructure at the pellet periphery, as discussed in section 2.3. The formation of a high-burnup rim zone is not modelled in FRAPCON-3.2, and the microstructural data required for the rim zone by SCANAIR are therefore estimated from experimental studies reported in literature as follows:

The width of the rim zone, w_{Rim} [µm], is in all analyses with SCANAIR correlated to the pellet radial average burnup, E_{av} [MWd(kgU)$^{-1}$], through

$$w_{Rim} = \begin{cases} 0 & E_{av} \leq 35, \\ 4.27 \cdot 10^{-2} \left(E_{av} - 35\right)^{2.41} & 35 < E_{av} < 70. \end{cases} \tag{3.1}$$

Equation (3.1) is a fit to optical microscopy data from post-irradiation examinations of commercial PWR fuel rods, presented by Manzel and Walker (2000; 2002). The material within the rim zone is assumed to have a uniform microstructure, the properties of which are defined in table 3.1. These properties are compiled from several studies on rim zone formation, which have been reviewed by Jernkvist and Massih (2002).

Fuel material property		**Rim zone**	**Low-burnup**
Density	[kgm^{-3}]	9670	10250
Porosity (volume fraction)	[-]	0.10	0.04
Grain size	[µm]	0.3	10
Intergranular bubble size	[nm]	2.0	20

Table 3.1: Rim zone microstructural properties applied in analyses with SCANAIR-3.2. Typical properties of low-burnup UO_2 fuel are also given for reference.

3.2.3.2 Clad-to-coolant heat transfer

Models in the SCANAIR-3.2 computer code cater for heat transfer from the clad tube to the surrounding coolant, consisting of either liquid sodium or liquid water (Federici et al., 2000). For the purpose of our analyses, we have equipped SCANAIR-3.2 with an extended coolant channel model, allowing for two-phase flow and thus for simulations of BWR operating conditions. In the extended model, which is fashioned after the coolant channel model in the FRAPTRAN computer code (Cunningham et al., 2001), the two-phase water coolant is treated as a homogeneous mixture of liquid and steam in thermodynamic equilibrium. The model has an extended set of clad-to-water heat transfer correlations, which is applicable to both PWR and BWR conditions. In table 3.2, the new set of correlations is compared with the standard models for clad-to-water heat transfer in SCANAIR-3.2. Most of the correlations in table 3.2 are described in a review of heat transfer correlations for light water reactor application, which has recently been published by the IAEA (2001).

Heat transfer regime	Standard SCANAIR-3.2	Extended SCANAIR-3.2
Forced convection to liquid phase	Dittus-Boelter	Dittus-Boelter
Subcooled nucleate boiling	Thom	Thom
Saturated nucleate boiling	-	Chen
Film boiling	Bishop-Sandberg-Tong	Groeneveld
Transition boiling	-	Condie-Bengtson
Forced convection to vapour phase	-	Dittus-Boelter
Critical heat flux	Babcock & Wilcox	EPRI-Columbia

Table 3.2: Clad-to-water heat transfer correlations used in SCANAIR-3.2. For a description of these correlations, see (IAEA, 2001).

3.2.3.3 Fuel pellet thermal conductivity

Two thermo-physical properties of the fuel pellets are of particular importance, when assessing enthalpy limits for fuel pellet melting under RIA: the solidus (melting) temperature and the thermal conductivity. The model for UO_2 solidus temperature in SCANAIR-3.2 is described and shortly reviewed in appendix C. In the present analyses, the model is used without modifications.

The model for UO_2 thermal conductivity in SCANAIR-3.2, however, was slightly modified for the purpose of our analyses. As described in appendix D, the modification was made since the model was found to overestimate recent experimental data on thermal conductivity of un-irradiated UO_2 by Ronchi et al. (1999).

3.3 Input

The input data to our thermo-mechanical analyses of postulated RIAs are partly based on core kinetics analyses, which were performed with the three-dimensional time-dependent neutronics code SIMULATE-3K by Vattenfall and OKG in an earlier part of this project, and we therefore apply much the same input as was used in these analyses. Hence, for the postulated rod ejection accident in PWRs, we assume the same fuel design and core conditions as applied by Gabrielson (2004) in analyses of HZP REA in Ringhals 3, a 3-loop PWR of Westinghouse design. For the postulated control rod drop accident in BWRs, we assume the same fuel design and core conditions as applied by Wiksell (2003) in analyses of CZP CRDA in Oskarshamn 3, an internal pump BWR of ASEA-ATOM design. It should be noticed, that the input used in the present analyses is identical to that applied in our companion assessment of fuel rod failure thresholds for RIA (Jernkvist & Massih, 2004).

3.3.1 Fuel rod design

The fuel considered in analyses of PWR HZP REA is a standard 17×17 design (Gabrielson, 2004). In analyses of BWR CZP CRDA, the fuel design is 10×10 (Wiksell, 2003). Key properties of these fuel designs are summarized in table 3.3.

Design parameter		PWR fuel rod (17×17)	BWR fuel rod (10×10)
Fuel rod active length	[mm]	3658	3680
Fuel rod pitch	[mm]	12.6	13.0
Fuel rod fill gas		He	He
Fill gas pressure	[MPa]	2.50	0.60
Fuel pellet material		UO_2	UO_2
Fuel pellet density	[% of theoretical]	95.0	96.7
Enrichment of ^{235}U	[%]	3.80	4.00
Fuel pellet diameter	[mm]	8.165	8.480
Pellet dish volume fraction	[%]	1.40	1.12
Clad tube material		Zircaloy-4 (SRA)	Zircaloy-2 (RX)
Clad outer diameter	[mm]	9.550	9.840
Clad wall thickness	[mm]	0.610	0.605

Table 3.3: Fuel rod designs considered in analyses.
SRA: Stress relieved annealed. RX: Recrystallized.

3.3.2 Steady-state base irradiation

The steady-state base irradiation is simulated by use of FRAPCON-3.2. Core cooling conditions corresponding to nominal conditions in the Ringhals 3 PWR and the Oskarshamn 3 BWR are assumed in these simulations; see table 3.4. The postulated steady-state power histories and axial power distributions are given in appendix E. The axial power distributions are assumed not to change during the irradiation history.

For the PWR fuel rod, a rod average linear heat generation rate (LHGR) of 23 kWm^{-1} is assumed for the first 290 effective full power days of operation, followed by a linear decrease in power with time, ending at 8.73 kWm^{-1} after 2000 days of reactor operation. A similar base irradiation is assumed for the BWR fuel rod: following 250 effective full power days at a constant rod average LHGR of 25 kWm^{-1}, the power decreases linearly with time, ending at 8.17 kWm^{-1} after 1800 days.

Parameter		PWR	BWR
Nominal thermal power	[MW]	2775	3020
Average linear heat generation rate	[kWm^{-1}]	18.3	12.7
Coolant pressure	[MPa]	15.5	7.0
Coolant inlet temperature	[K]	557	550
Subchannel mass flow	[gs^{-1}]	327.5	174.6
Subchannel mass flux	[$kg(m^2s)^{-1}$]	3759	1878

Table 3.4: Core conditions applied in simulations of fuel rod base irradiation. These are nominal conditions of the Ringhals 3 and Oskarshamn 3 power plants, respectively. The coolant subchannel pertains to a single fuel rod.

3.3.3 Postulated reactivity initiated accidents

The assumptions made about the reactivity initiated accidents in our analyses with SCANAIR-3.2 are based on the results of three-dimensional core kinetics analyses reported by Gabrielson (2004) and Wiksell (2003). Their analyses of postulated RIAs with SIMULATE-3K provided a spectrum of power pulses, with large variations in shape. This is illustrated in figures 3.2 and 3.3, which show calculated pulse widths and normalized pulse shapes from the performed analyses of HZP REA and CZP CRDA (In de Betou et al., 2004).

To avoid the use of multiple pulse shapes in analyses of the thermo-mechanical fuel rod behaviour under RIA, a Gaussian power pulse is used in all analyses with SCANAIR. As shown in figure 3.3, the Gaussian pulse constitutes an envelop to the calculated pulse shapes. Moreover, the full width at half maximum of the applied Gaussian power pulse is set to 25 ms in analyses of HZP REA and to 45 ms in analyses of CZP CRDA. These pulse widths are taken from the lower end of the results presented in figure 3.2.

The core conditions applied under RIA are defined in table 3.5. They are identical to the conditions used in the core kinetics analyses by Gabrielson (2004) and Wiksell (2003). It should be noticed that the very low initial rod power leads to fuel and clad tube temperatures, prior to RIA, that are very close to the coolant inlet temperature. Moreover, the coolant outlet temperature does not differ notably from the inlet temperature.

The distributions of generated power along the fuel rod under the considered RIAs are prescribed in a penalizing manner, and do not reflect the true power distribution. The axial power distributions postulated for the PWR HZP REA and the BWR CZP CRDA in our analyses are shown in figure 3.4. The power distributions, which are assumed not to change during the transient, closely follow the calculated axial variations in clad oxide layer thickness along the fuel rods. Accordingly, the peak power under RIA is concentrated at the axial position of peak clad corrosion. As a consequence of these postulated axial power distributions, fuel pellet melting is predicted always to occur at the axial position of peak clad corrosion. This results in conservative estimates of the core failure limit, since the calculated enthalpy for fuel pellet melting decreases slightly with increasing oxide thickness. This is further discussed in section 5.1.

Parameter		**PWR HZP REA**	**BWR CZP CRDA**
Initial power	[% of nominal]	0.1	0.01
Coolant pressure	[MPa]	15.5	0.1
Coolant inlet temperature	[K]	564.9	303.1
Subchannel mass flow	[gs^{-1}]	327.5	61.1
Subchannel mass flux	[$kg(m^2s)^{-1}$]	3759	657.2

Table 3.5: Core conditions applied in simulations of reactivity initiated accidents. The coolant subchannel pertains to a single fuel rod.

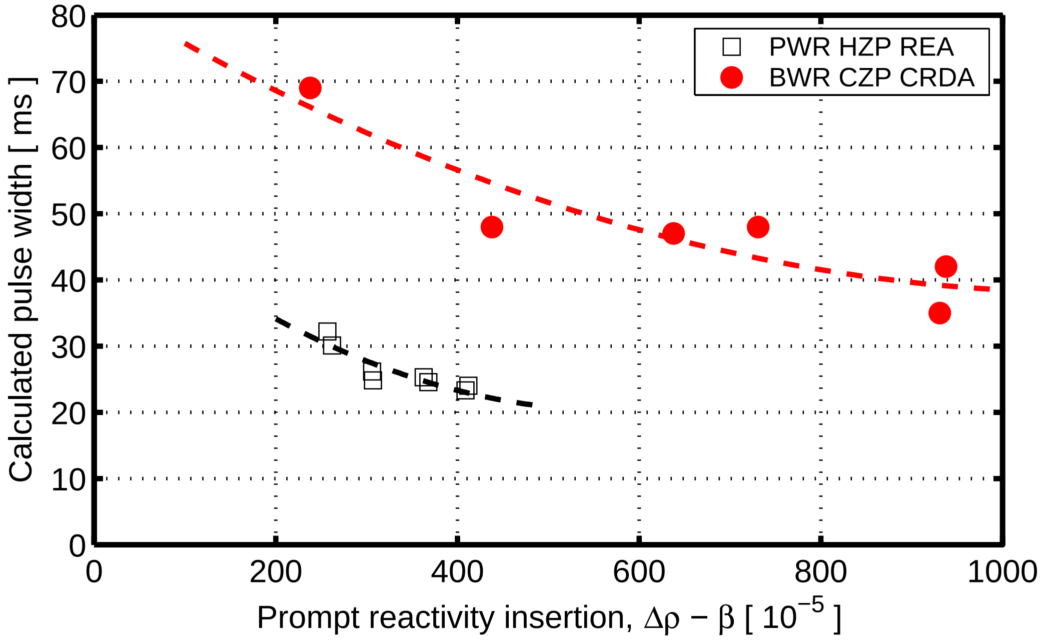

Figure 3.2: Calculated pulse widths. Here, Δρ is the inserted reactivity, and β is the delayed neutron fraction (In de Betou et al., 2004).

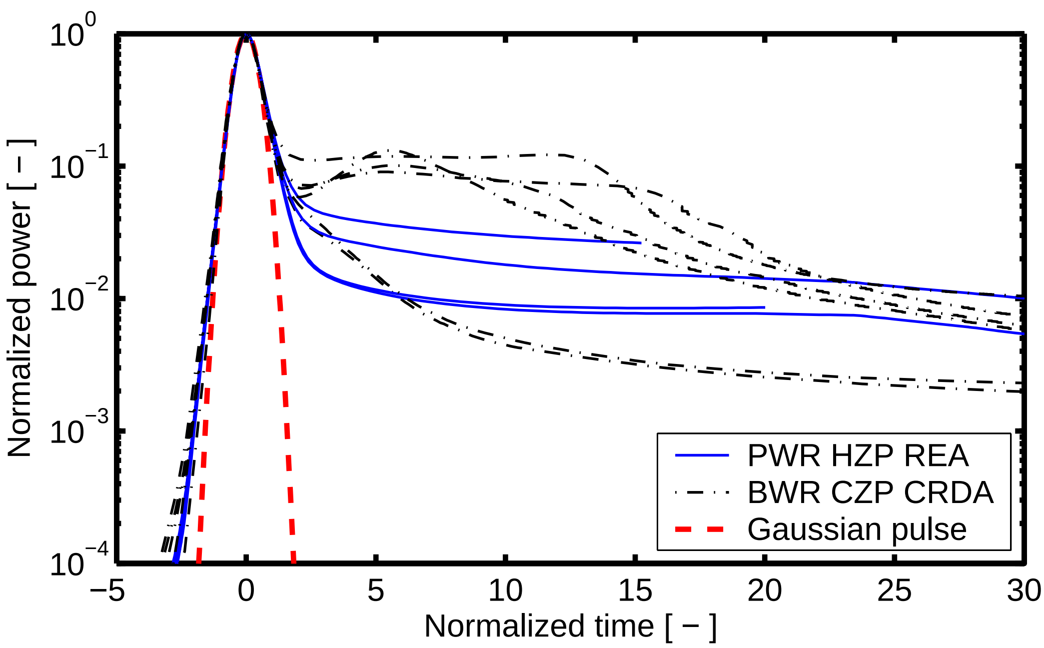

Figure 3.3: Calculated power pulses from three-dimensional core kinetics analyses in comparison with Gaussian pulse. The pulses are normalized (In de Betou et al., 2004).

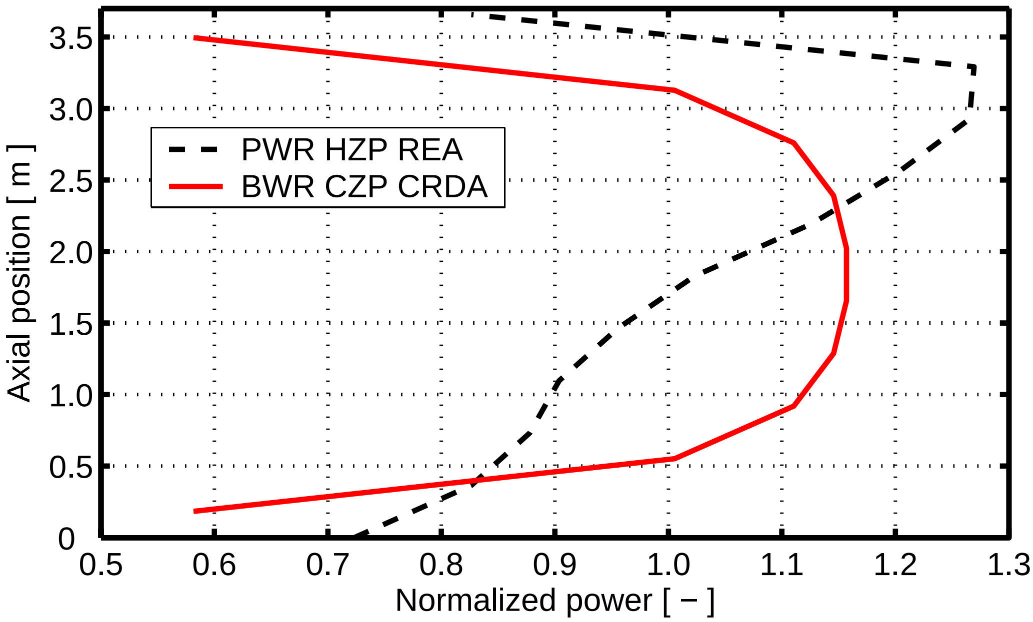

Figure 3.4: Fuel rod axial power distributions assumed under postulated RIAs. The power distributions are postulated in a penalizing manner, such that peak power is concentrated at the axial position of peak clad corrosion.

4 Results

Calculated burnup dependent fuel rod conditions prior to RIA are given in section 4.1. These calculated conditions serve as input to the transient analyses of the actual RIA, the results of which are compiled in section 4.2.

4.1 Calculated fuel rod conditions prior to RIA

Key results from the simulated base irradiation of the PWR and BWR fuel rods are summarized in table 4.1. The simulations were performed with the FRAPCON-3.2 computer code, using best-estimate models.

Parameter		PWR rod	BWR rod
Rod average burnup	[$MWd(kgU)^{-1}$]	70.7	60.6
Rod axial peak burnup	[$MWd(kgU)^{-1}$]	80.1	70.1
Fission gas release	[%]	3.72	2.85
Peak clad oxide thickness	[μm]	74.1	28.6
Peak clad hydrogen content	[wppm]	555	420

Table 4.1: Calculated fuel rod properties at end of base irradiation.

The calculated evolution of clad corrosion and pellet-clad gap conditions are presented in the sequel. These data pertain to the rod axial segment at which fuel pellet melting is predicted to occur, i.e. to the axial position of peak power and peak clad corrosion; confer section 3.3.3. For the PWR fuel rod, this is the 9^{th} axial segment out of 10, corresponding to an axial elevation of 2.9-3.3 m from bottom of the rod. For the BWR fuel rod, fuel pellet melting is predicted to occur in the 6^{th} axial segment of the rod, corresponding to an axial elevation of 1.8-2.2 m.

4.1.1 Clad corrosion

Figure 4.1 shows the calculated local clad oxide thickness with respect to local burnup in the peak oxide axial segment of the PWR and BWR fuel rods. The corrosion is calculated by use of best-estimate models for standard Zircaloy-2 and Zircaloy-4 cladding in FRAPCON-3.2 (Berna et al., 1997).

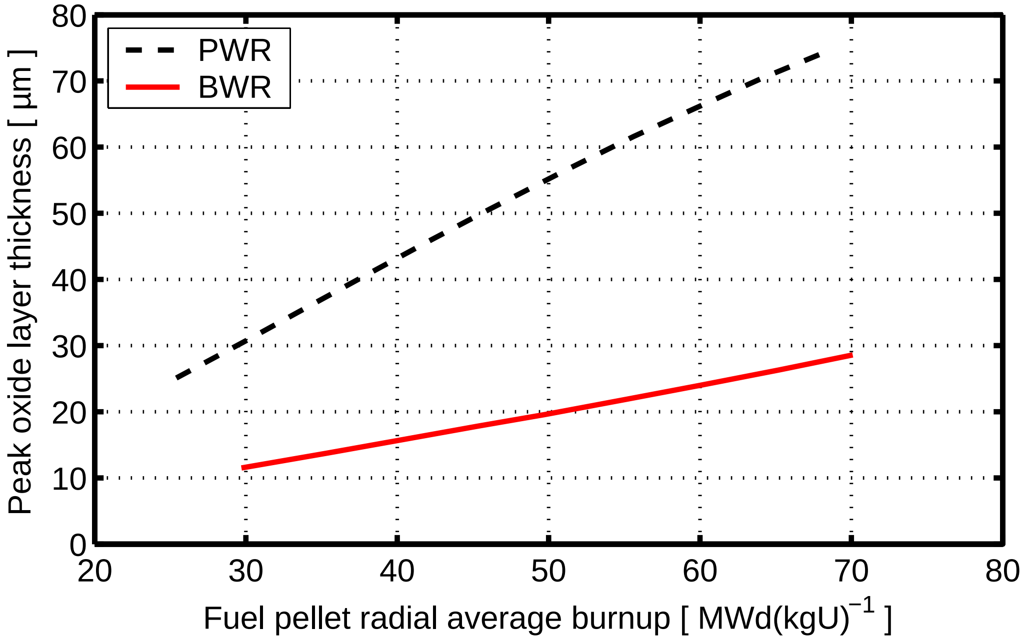

Figure 4.1: Local clad oxide layer thickness with respect to local burnup in the peak oxide axial segment, calculated with best-estimate models in FRAPCON-3.2.

4.1.2 Pellet-clad mechanical interaction

Figures 4.2 and 4.3 show the calculated radial pellet-clad gap size and contact pressure prior to RIA with respect to local burnup in the peak oxide axial segment of the PWR and BWR fuel rod, respectively. Hence, the presented gap conditions are calculated at hot zero power for the PWR rod, and at cold zero power for the BWR rod. Obviously, the pellet-clad gap closes at a burnup of 38 MWd(kgU)$^{-1}$ in the PWR fuel rod, whereas it remains open up to 60 MWd(kgU)$^{-1}$ in the BWR rod. This is partly due to the difference in clad creep down between PWR and BWR fuel rods, but also the difference in pre-transient coolant pressure (15.5 and 0.1 MPa, respectively) contributes to the disparity in initial pellet-clad gap size.

4.1.3 Pellet-clad heat transfer

Figure 4.4 shows the calculated pellet-clad heat transfer coefficient prior to RIA with respect to local burnup in the peak oxide axial segment of the PWR and BWR fuel rods. The heat transfer coefficient is significantly higher for the PWR fuel rod, which is due mainly to the difference in initial temperature of the gap gas between the PWR and BWR fuel rod. As shown in table 3.5, both the initial coolant temperature and fuel rod power is higher for the PWR fuel rod, which results in higher temperature and improved thermal conductivity for the gas within the pellet-clad gap.

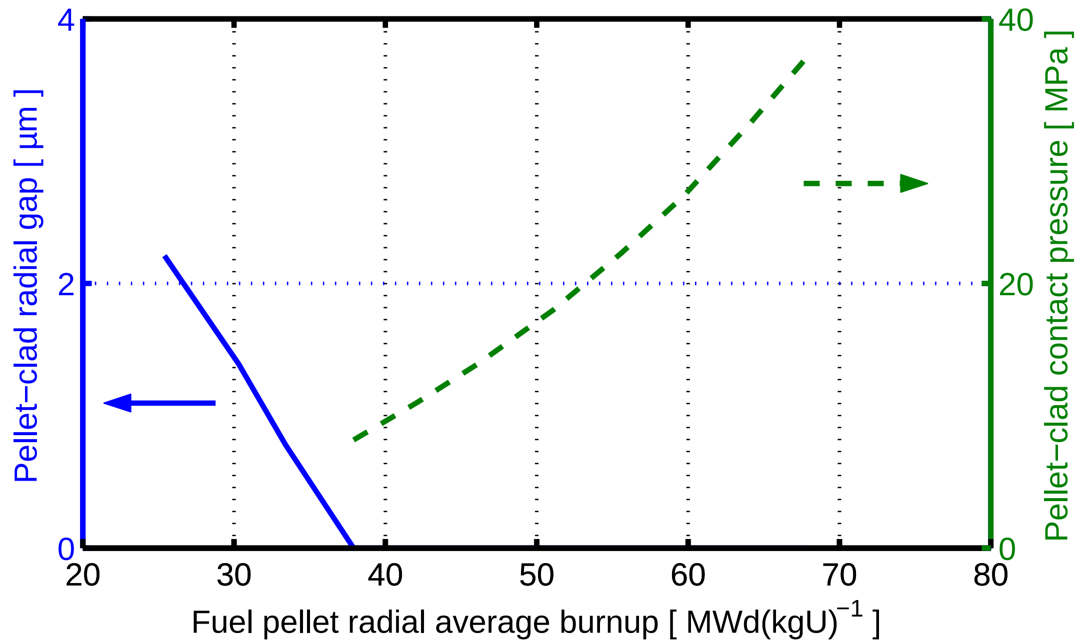

Figure 4.2: Calculated pre-transient pellet-clad radial gap size and contact pressure with respect to local burnup in the peak oxide axial segment of the PWR fuel rod. The gap is calculated at hot zero power, as defined in table 3.5: i.e. for near zero power, coolant pressure of 15.5 MPa and coolant temperature 565 K.

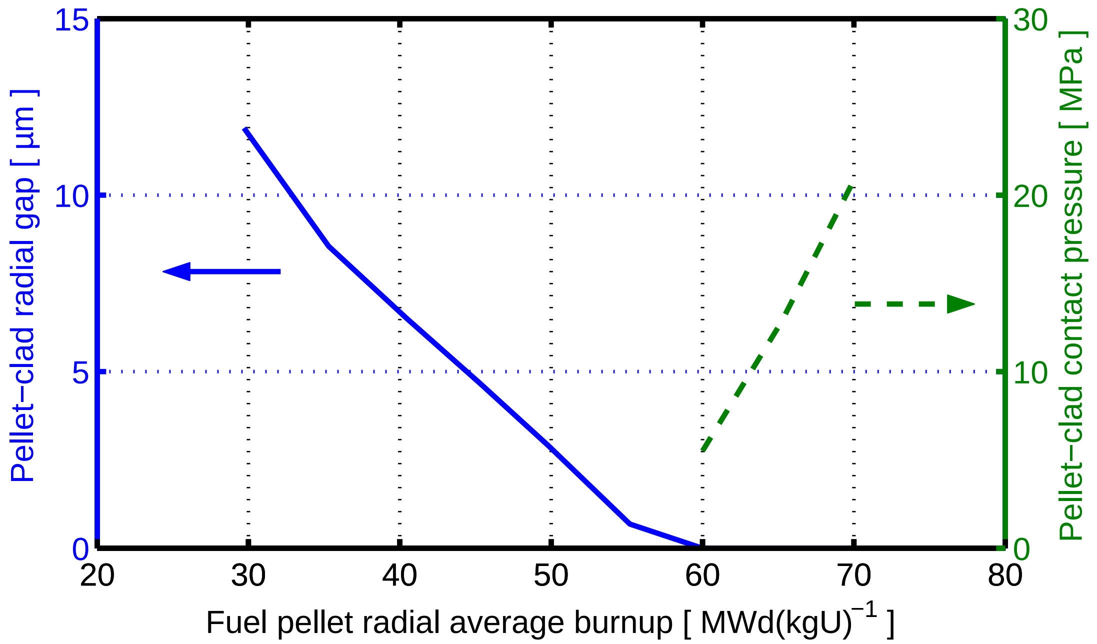

Figure 4.3: Calculated pre-transient pellet-clad radial gap size and contact pressure with respect to local burnup in the peak oxide axial segment of the BWR fuel rod. The gap is calculated at cold zero power conditions, as defined in table 3.5: i.e. for near zero power, coolant pressure of 0.1 MPa and coolant temperature of 303 K.

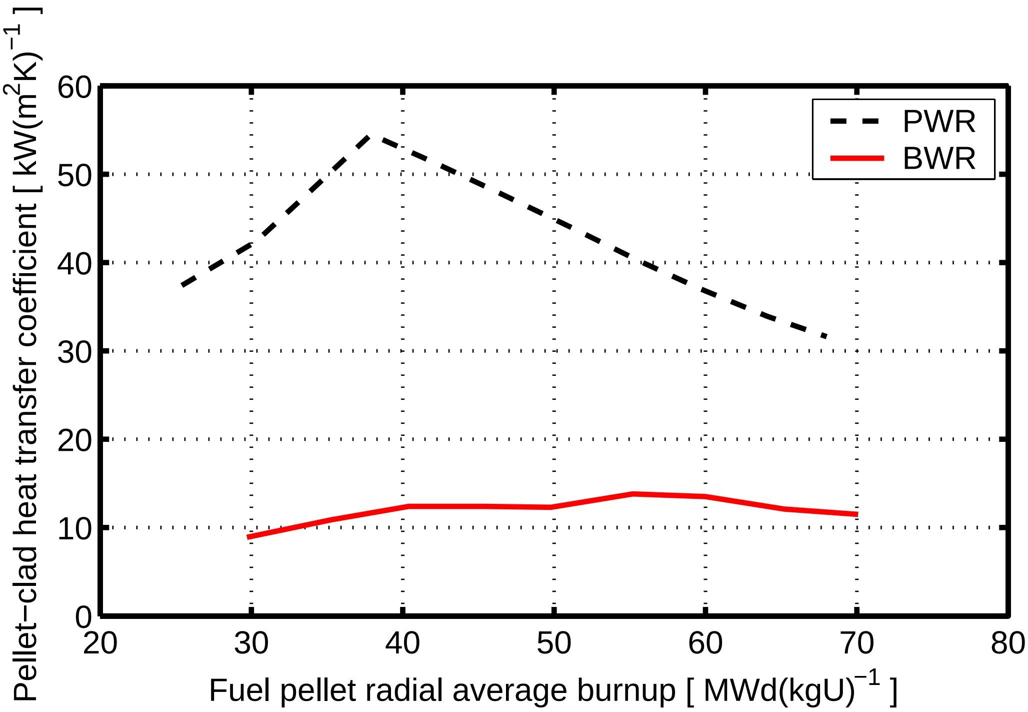

Figure 4.4: Calculated pellet-clad heat transfer coefficient prior to RIA with respect to local burnup in the peak oxide axial segment. The difference between the PWR and BWR rod is caused mainly by differences in gap gas temperature prior to RIA.

4.2 Calculated fuel rod conditions under RIA

Key results from the performed analyses of RIA with SCANAIR-3.2 are presented graphically in the sequel. The same data are given in tabular form in appendix F. This appendix also contains some complementary data, which are not presented in the graphs below. It should once again be pointed out, that all data pertain to the rod axial segment in which fuel pellet melting is predicted to occur, i.e. to the axial position of peak power, peak fuel enthalpy and peak clad corrosion; confer section 3.3.3. For the PWR fuel rod, this is the 9th axial segment out of 10, corresponding to an axial elevation of 2.9-3.3 m from bottom of the rod. For the BWR fuel rod, pellet melting is predicted to occur in the 6th axial segment of the rod, at an axial elevation of 1.8-2.2 m.

4.2.1 Core failure limits

Figure 4.5 shows the calculated enthalpy thresholds for fuel pellet melting in terms of peak radial average fuel enthalpy under the power pulse, plotted with respect to fuel pellet burnup in the rod axial segment at which melting is predicted. Hence, the enthalpy shown in figure 4.5 is *not* necessarily the fuel enthalpy at time of melting, but the peak value obtained under a power pulse with sufficient amplitude to just reach the fuel solidus temperature at a single point in the discretized fuel rod.

In the PWR fuel rod, fuel pellet melting is predicted to occur 0-5 ms before the peak fuel enthalpy is reached, depending on burnup, whereas for the BWR fuel rod, pellet melting occurs 0-14 ms before the peak fuel enthalpy is attained. Further information on this issue is given in appendix F.

All enthalpies are calculated with respect to a reference temperature of 273 K. The calculated initial fuel enthalpy, prior to the postulated RIA, is 72.9 $J(gUO_2)^{-1}$ for the PWR fuel rod and 2.6 $J(gUO_2)^{-1}$ for the BWR rod. The peak fuel enthalpy is reached approximately 25 ms after peak power in the PWR rod, and the corresponding time lag is about 50 ms for the BWR rod.

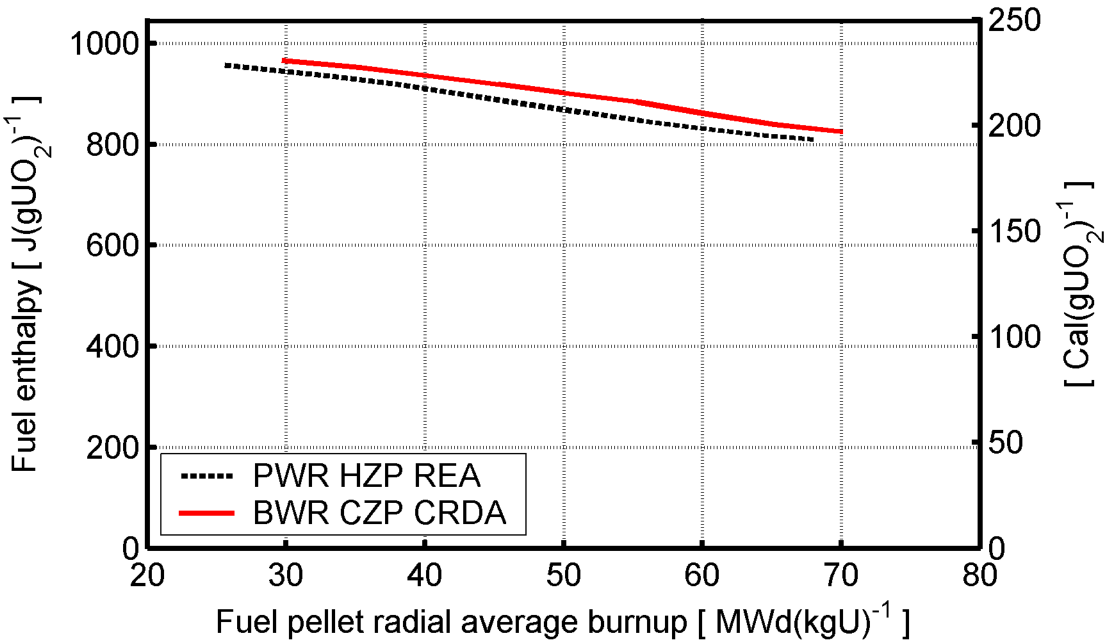

Figure 4.5: Calculated core failure limits for HZP REA and CZP CRDA. The fuel enthalpy is the threshold for incipient fuel pellet melting, in terms of peak radial average value during the power pulse.

4.2.2 Fuel temperatures at incipient melting

The calculated local fuel temperatures at incipient melting are shown in figure 4.6. These temperatures are peak values with respect to both time and space, and they are tabulated in appendix F. As already mentioned, the peak fuel temperatures and enthalpies are always reached in the 9^{th} axial segment of the PWR rod, and in the 6^{th} segment of the BWR rod.

From figure 4.6, it is evident that the local temperatures at incipient fuel pellet melting differ by less than 2 K between the PWR and BWR fuel rods, when plotted with respect to fuel pellet radial average burnup. The difference is due to the fact that the radial distribution of burnup is slightly more peaked in the PWR than in the BWR fuel rod, for the fuel designs considered in our analyses.

For a certain fuel pellet radial average burnup, the radial peak burnup is therefore higher in the PWR rod, and the local fuel temperature at incipient melting somewhat lower.

The calculated peak fuel temperature is found about 0.25 mm beneath the fuel pellet surface. However, the peak temperature position moves slightly outward with increasing burnup, as a result of the change in radial power distribution. This burnup dependent change in radial temperature profile is illustrated in figures 4.7 and 4.8, which show the calculated variation in fuel temperature across the pellet radius at time of incipient fuel melting in low- and high-burnup fuel. The temperature profiles at high burnup are strongly peaked to the region just beneath the pellet surface.

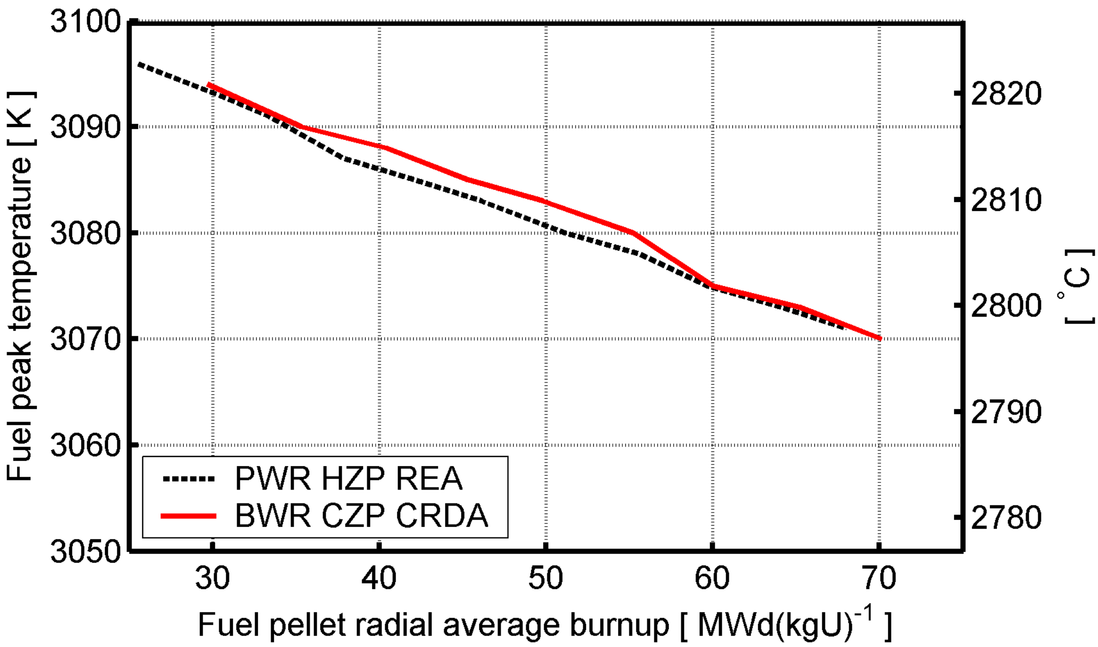

Figure 4.6: Calculated local fuel temperatures at incipient fuel pellet melting for PWR HZP REA and BWR CZP CRDA. These fuel temperatures are peak values with respect to both space and time; see tables F.1 and F.2 in appendix F.

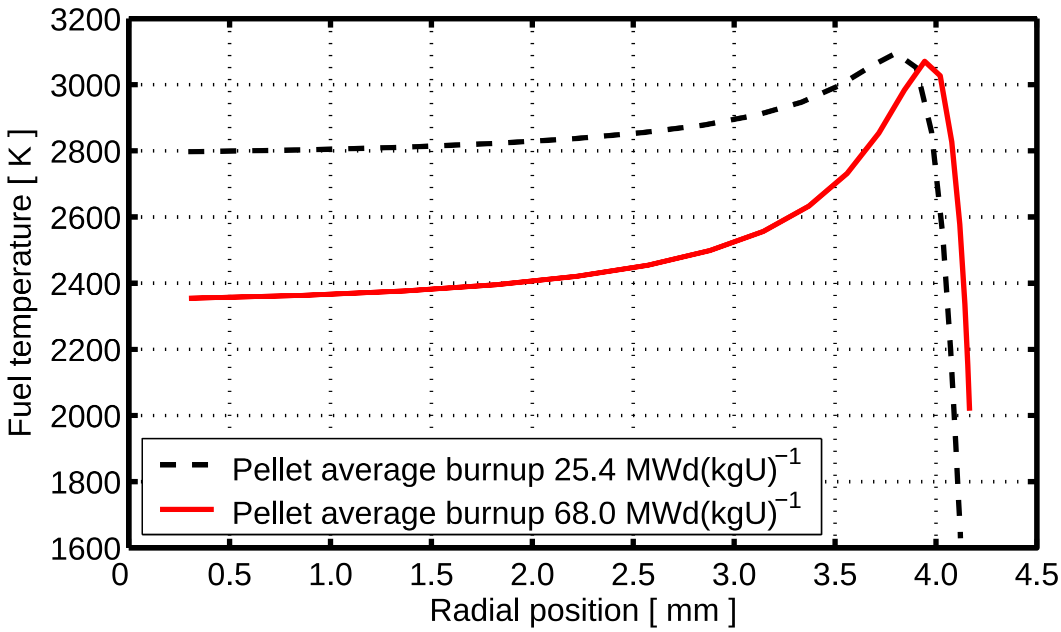

Figure 4.7: Calculated variation in fuel temperature across the pellet radius at time of incipient fuel melting under the PWR HZP REA. The temperature profile is shown for low- and high-burnup fuel, and pertains to the peak power axial segment of the fuel rod.

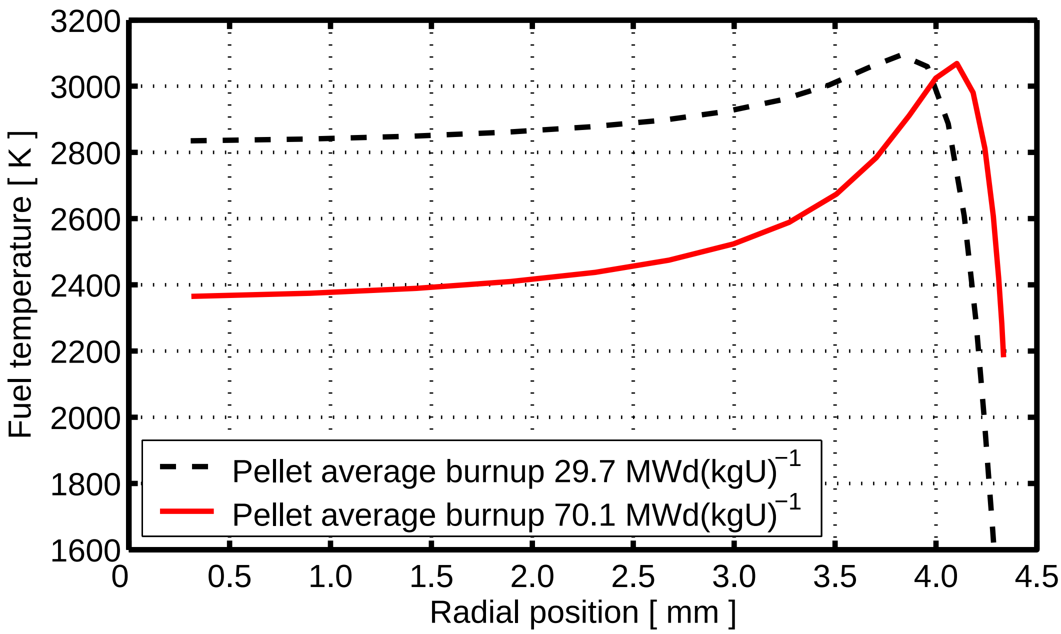

Figure 4.8: Calculated variation in fuel temperature across the pellet radius at time of incipient fuel melting under the BWR CZP CRDA. The temperature profile is shown for low- and high-burnup fuel, and pertains to the peak power axial segment of the fuel rod.

5 Discussion

The calculated core failure limits presented in section 4.2.1 should not be viewed as definite operational limits for the reactor core, but merely as best-estimate assessments of the influence of fuel rod burnup on the enthalpy to fuel melting under RIA. The applicability of the calculated failure limits is discussed in section 5.1, where also the limitations of the performed analyses are defined. The calculated core failure limits are further evaluated in section 5.2, where comparisons are made with the current core failure limit for RIA in Sweden. A comparison is also made with a calculated core failure limit for high-burnup fuel rods under RIA, which has recently been presented by the Electric Power Research Institute (EPRI) in the USA. Finally, in order to define operational limits with respect to core failure under RIA, one must consider not only fuel melting, but also the potential for dispersal of large amounts of non-molten fuel fragments from failed high-burnup fuel rods. This is further discussed in section 5.3.

5.1 Applicability of calculated core failure limits

Firstly, it should be noticed that the calculated core failure limits in this report are defined with respect to the radial average fuel burnup in the rod axial segment at which incipient fuel melting is predicted, and not with respect to the rod *average* burnup. By using local rather than average fuel burnup, comparisons of the calculated failure limits with pulse reactor tests on short-length rodlets are made easier. The local burnup in the axial segment at which pellet melting occurs, E_{loc}, is in the performed analyses related to the rod average burnup, E_{rod}, through

$$E_{loc} \quad = \quad C\,E_{rod}\ , \qquad (5.1)$$

where the local-to-average burnup factor C is 0.961 for the PWR rod, and 1.157 for the BWR rod, respectively. Hence, due to the upper-peaked power profile imposed on the PWR fuel rod under REA, fuel pellet incipient melting is predicted in the upper part of the rod, where the local burnup is slightly lower than the rod average value; see figure 3.4 and figure E.2 in appendix E.

The postulated HZP REA and CZP CRDA considered in our calculations result in lower enthalpies for pellet melting than RIAs that take place at rated power. Consequently, scenarios for RIA at rated power are conservatively bounded by the calculated enthalpy limits. As a rule, any effect or phenomenon that makes the fuel radial temperature profile more peaked to the pellet periphery will lower the calculated enthalpy limits, since a certain peak temperature is reached at a lower radial average fuel enthalpy. For this reason, our calculations were performed with low fuel enrichments, near-zero initial power, narrow pulse widths and thick clad oxide layers. These conditions make the fuel temperature profile strongly peaked to the pellet periphery, and the calculated radial average fuel enthalpies for pellet melting are therefore low.

The failure limits in section 4.2.1 are calculated for typical LWR fuel designs, as defined in table 3.3.

It should be emphasised, that the failure limits are calculated for fuel rods with UO_2 fuel pellets, and that they are not applicable to $(U,Pu)O_2$ mixed oxide (MOX) fuel rods. The MOX fuel material has lower thermal conductivity and melting temperature than UO_2 fuel, and the radial power distribution within the MOX fuel pellets is different from that in UO_2 fuel. This difference is important for the prediction of incipient fuel melting, since it affects the temperature distribution across the fuel pellet radius.

The calculated core failure limits are for the same reasons not applicable to burnable absorber (BA) fuel, which usually contains 3-8 wt% Gd_2O_3. Enthalpy thresholds for incipient fuel pellet melting in MOX and BA fuel rods may be calculated essentially in the same fashion as for UO_2 fuel rods, but additional models for radial distribution of power, thermal conductivity and melting temperature must first be introduced into the computer codes for these kinds of fuel.

The calculated core failure limits in section 4.2.1 depend on the applied UO_2 melting temperature, and in particular on how the burnup dependent depression of the melting point is modelled. The model used in our analyses is the default correlation for UO_2 solidus temperature in SCANAIR-3.2, which predicts a fairly moderate depression of melting temperature with increasing burnup. As discussed in appendix C, there are experimental data from the sixties that would suggest a more substantial depression, but there seems to be a consensus that these early data are misleading, due to inadequate experimental techniques; see e.g. the reviews by Fink (1996), Popov et al. (2000) and Carbajo et al. (2001). We have not been able to compare the model for UO_2 melting temperature in SCANAIR-3.2 with contemporary data on irradiated fuel, since, to our knowledge, such data are unavailable in open literature. However, the model agrees quite well with a correlation proposed by Komatsu et al. (1988), and it has therefore been applied without modifications in our analyses; see appendix C.

The calculations in our study are made with best-estimate computer models and methods, but it should be noticed that penalizing assumptions are made concerning the postulated power transients under RIA. Firstly, a Gaussian pulse shape is used in our analyses, which leads to faster energy depositions than if realistic pulse shapes, obtained from the core kinetics analyses by Gabrielson (2004) and Wiksell (2003), are used. Secondly, the applied pulse widths, 25 and 45 ms for PWR and BWR, respectively, correspond to lower-end results from the above mentioned core kinetics analyses; see figure 3.2. These narrow pulses result in fast energy deposition in the fuel, which lowers the calculated enthalpy thresholds for pellet incipient melting. Thirdly, the axial power distributions are postulated in a penalizing manner, such that the peak power under RIA is concentrated at the axial position of peak clad corrosion. These penalizing assumptions are made in order to account for the uncertainties associated with the power generation in high-burnup fuel under RIA.

5.2 Evaluation of calculated core failure limits

5.2.1 Comparison with current core failure limit

The calculated core failure limits for PWR HZP REA and BWR CZP CRDA from section 4.2.1 are in figure 5.1 compared with the current core failure limit for RIA in Sweden (SKI, 1995). Obviously, the calculated threshold enthalpies for incipient fuel melting agree very well with the current failure limit for low- and intermediate burnup, i.e. below the breakpoint for the current failure limit at 37.4 $MWd(kgU)^{-1}$. For higher burnup, the current core failure limit is set with attention to dispersion of non-molten fuel fragments from failed rods, rather than fuel melting, and it is therefore not comparable to our calculated enthalpy limits. This is further discussed in section 5.3.

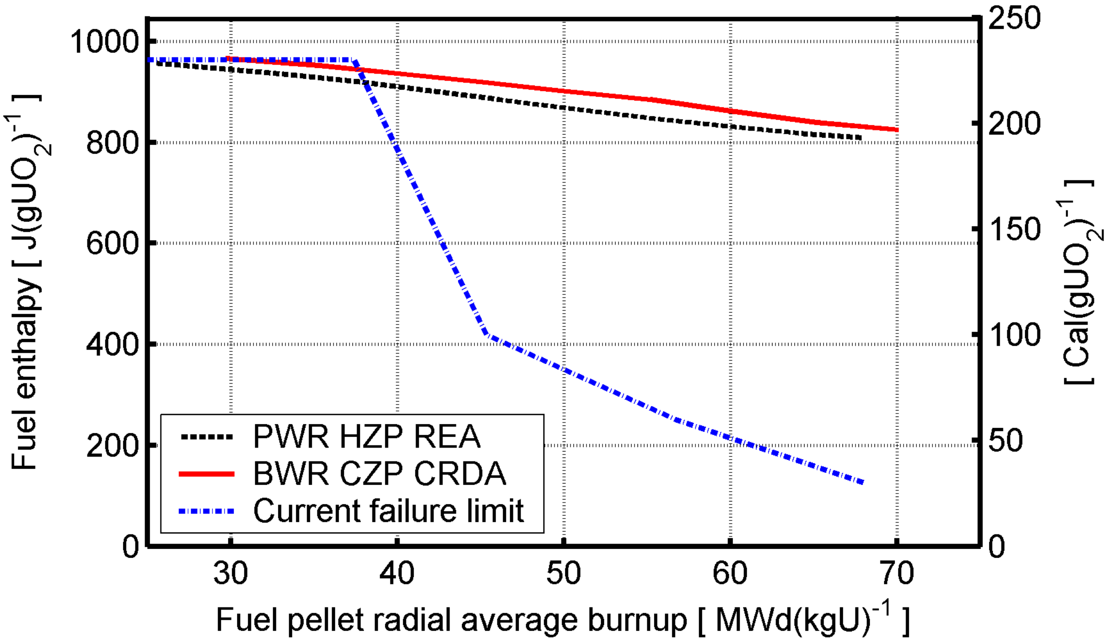

Figure 5.1: Calculated core failure limits, in comparison with the current core failure limit for RIA in Sweden; see appendix A.

The calculated core failure limits drop moderately with increasing fuel burnup, and notwithstanding the differences in fuel rod designs and postulated accident scenarios between the PWR HZP REA and the BWR CZP CRDA considered in our analyses, the calculated failure limits for these two events are similar. The failure limit for the BWR CZP CRDA is slightly higher, mainly as a result of the wider power pulse. As revealed by figures 4.7 and 4.8, the wider power pulse in the BWR event in comparison with the PWR REA leads to a somewhat more uniform temperature profile across the fuel pellet radius. Consequently, for the same radial peak temperature, the pellet radial average fuel enthalpy will be higher in the BWR than in the PWR fuel rod.

The calculated enthalpy limits decrease gradually with fuel burnup, from approximately 960 $J(gUO_2)^{-1}$ at 30 $MWd(kgU)^{-1}$ to 810 $J(gUO_2)^{-1}$ at 70 $MWd(kgU)^{-1}$. The decrease is partly due to depression of the fuel melting temperature with burnup, as illustrated by figure 4.6 and further discussed in appendix C. However, the burnup dependent change in radial distribution of power and temperature within the pellet also contributes to the drop in calculated enthalpy to fuel melting. As shown in figures 4.7 and 4.8, the radial temperature profile is strongly peaked to the pellet periphery at high burnup, which means that a certain peak temperature is reached at a lower radial average fuel enthalpy at high burnup than at low burnup.

5.2.2 Comparison with study done by EPRI/ANATECH

It is interesting to compare our calculated core failure limits with the results of a similar study, which has recently been done for PWR rod ejection accidents at hot zero power conditions by ANATECH Corporation, under the auspices of EPRI (Yang et al., 2003). All fuel rod analyses in this study were performed with the FALCON computer code, which in contrast to FRAPCON-3.2 is applicable to both steady-state and transient fuel rod analyses. The assumed power transient under the REA was a 20 ms wide Gaussian power pulse, and a core failure limit was calculated, using fuel pellet incipient melting as failure criterion. Hence, the analyses made by ANATECH were very similar to those in the present report. Except for the slightly narrower power pulse, 20 instead of 25 ms, the differences to our analyses are confined to the applied models and computer codes. The calculated core failure limit from the study by EPRI/ANATECH is compared with the results of our analyses of PWR HZP REA in figure 5.2. As can be seen from the figure, these calculated core failure limits are in close agreement, and they follow the same trend with respect to fuel burnup.

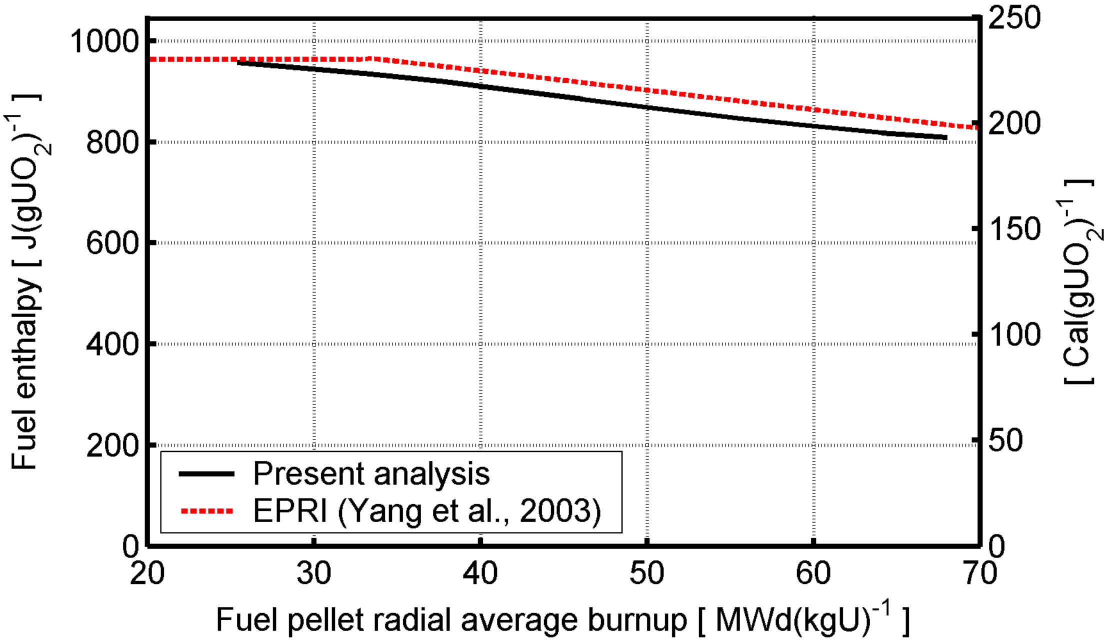

Figure 5.2: Comparison of calculated core failure limits for PWR HZP REA.

The calculated enthalpies to fuel pellet melting are about 30 $J(gUO_2)^{-1}$ lower in our analyses than in the study by EPRI/ANATECH. This difference is by no means remarkable, and may be explained by differences in the applied models and computer codes. In fact, the discrepancy of 30 $J(gUO_2)^{-1}$ is probably a good estimate of model-induced uncertainties in the performed analyses.

It should be pointed out, that the core failure limit calculated by EPRI/ANATECH is said to be applicable to both BWR and PWR fuel rods, which are subjected to reactivity initiated accidents that initiate from hot reactor conditions. The limit was recently introduced in Switzerland as a regulatory acceptance criterion for RIA under PWR and BWR hot reactor conditions by the Swiss Federal Nuclear Safety Inspectorate (Maeder & Wand, 2004).

5.3 Dispersal of high-burnup fuel

The core failure limits presented in this report are calculated peak radial average fuel pellet enthalpies connected with incipient UO_2 melting under RIA. By precluding fuel melting, pulse reactor tests on fresh fuel have shown that fuel dispersal into the coolant is avoided, and that core coolability and reactor pressure vessel integrity can be ensured. However, as discussed in section 2.2, tests on high-burnup fuel rods indicate that the accumulation of gaseous fission products within the pellets may lead to additional fuel dispersal mechanisms for burnups exceeding approximately 40 $MWd(kgU)^{-1}$. With the computational tools at hand, we are unable to model these mechanisms, and a fuel dispersal limit for high-burnup fuel can therefore not be calculated. Moreover, it is difficult to establish such a limit also from pulse reactor tests, since the database of failed high-burnup test rods is meagre; see appendix B. To make matters worse, the power pulses and cooling conditions in the tests differ from those expected in commercial light water reactors under RIA, and fuel dispersal limits determined in pulse reactor tests are therefore not directly applicable to LWRs. The importance of prototypical test conditions is in fact underlined by the distinct differences in failure behaviour observed between pulse tests performed in CABRI and the NSRR, as discussed in section B.4.

However, with these reservations kept in mind, the results from pulse reactor tests on SPERT and NSRR-JMTR rods, ranging in burnup from 21 to 38 $MWd(kgU)^{-1}$, show that the potential for dispersion of non-molten fuel fragments from failed fuel rods is low at low and intermediate burnup. As shown by figure B.3 in appendix B, no or marginal fuel loss was observed for peak fuel enthalpies below 850 $J(gUO_2)^{-1}$ for these rods. The results are possibly biased by high ^{235}U enrichment in the rods (7, 10, 20 %) and atypical pre-irradiation conditions, but they still confirm that dispersal of non-molten fuel is primarily a high-burnup issue.

Concerning the pulse reactor tests on high-burnup fuel, i.e. in the range of 44 to 64 $MWd(kgU)^{-1}$, we first note that all these tests were carried out on samples, which were re-fabricated from commercial LWR fuel rods after 4-5 cycles of operation in power reactors. The results of the tests are therefore not biased by odd fuel designs or atypical pre-irradiation conditions. Although the failure behaviour differs considerably between rods tested in the NSRR and the CABRI reactor, the tests show that dispersion of non-molten fuel particles into the coolant cannot be precluded in this burnup interval.

As discussed in section 2.3, the current core failure limit for high-burnup fuel coincides with the fuel rod failure threshold, which means that clad tube failure is assumed to cause significant fuel dispersal (SKI, 1995). However, clad failure in high-burnup fuel rods does not inevitably lead to fuel dispersal. In the tests, the degree of fuel loss into the coolant is correlated to the failure mode of the clad tube: circumferential breaks result in large loss of fuel material in the tests, whereas the fuel loss is less than 10 % in tests where the clad tube failed by axial splits. The use of a common enthalpy threshold for clad tube failure and fuel dispersal is in other words not well supported by experimental data.

As shown in figure B.4, the experimental data suggest that a peak fuel enthalpy of at least 500 $J(gUO_2)^{-1}$ is required to expel a significant part of the fuel inventory from high-burnup fuel rods in these tests. It is yet difficult to draw any definite conclusions, since the database is restricted to only eleven failed high-burnup fuel rods, for which the degree of fuel pellet loss has been reported. Moreover, three of these tests should be discarded, since the rods failed in an atypical manner along the weld to the bottom end fitting; see appendix B.

Waeckel et al. (2000) analysed UO_2 fuel rods that failed in the CABRI tests, and proposed that there is a margin of at least 30 $cal(gUO_2)^{-1}$ (126 $J(gUO_2)^{-1}$) between clad failure and fuel dispersal. Hence, the enthalpy threshold for fuel dispersal should be at least 30 $cal(gUO_2)^{-1}$ higher than the threshold for clad tube failure. Similar ideas were also put forth by Yang et al. (2003), who proposed that the degree of fuel dispersal should be correlated to the energy deposition into the fuel *after* clad tube failure.

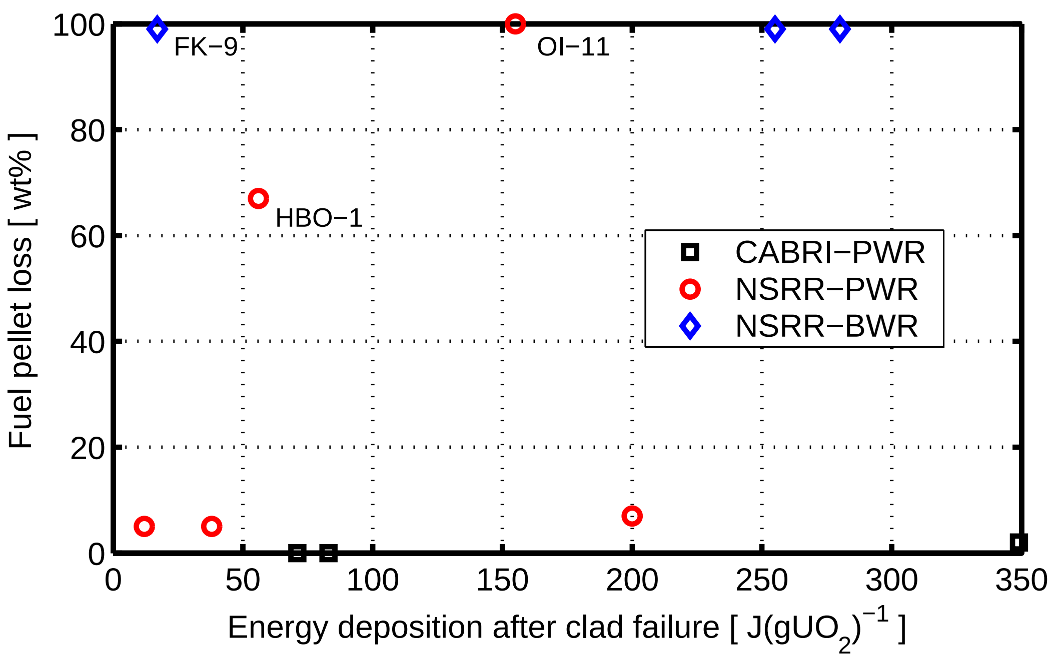

Figure 5.3: Measured fuel loss in failed high-burnup fuel rods, plotted with respect to energy deposition after clad failure. The fuel burnup of these rods range from 44 to 64 $MWd(kgU)^{-1}$. The rods HBO-1, FK-9 and OI-11 failed in the weld to the bottom end fitting, i.e. in an atypical mode of clad tube failure.

This hypothesis is tested against fuel dispersal data from failed high-burnup fuel rods in figure 5.3, which shows the measured fuel loss in failed high-burnup fuel rods, plotted with respect to energy deposition after clad failure. The latter quantity is here defined as the peak fuel enthalpy minus the enthalpy at clad failure. Obviously, the fuel pellet loss is poorly correlated to the energy deposition after failure in these eleven tests. A comparison of figure 5.3 with figure B.4 reveals that the fuel pellet loss seems more clearly correlated to peak fuel enthalpy than to energy deposition after clad failure.

As already mentioned, the tests conditions in CABRI and the NSRR are not prototypical with respect to pulse widths and cooling conditions, and the results of pulse tests in these facilities can therefore not be directly used to define enthalpy thresholds for fuel dispersal in light water reactors. The impact of pulse width on the mechanisms for clad tube failure and fuel pellet fragmentation is discussed in section B.4 of appendix B, and will not be addressed here. However, a comment should be made on the expected differences in fuel-coolant interaction between the pulse reactors and LWRs. Firstly, we note that the current test loop in CABRI uses liquid sodium as coolant. Since the boiling point of sodium is 1150 K, we do not expect significant amounts of sodium to be vaporized upon contact with dispersed fuel fragments. The fuel-coolant thermal interaction in CABRI is therefore not representative of that expected in an LWR.

The cooling conditions in the NSRR are compared with those assumed in our analyses of BWR CZP CRDA and PWR HZP REA in table 5.1. The coolant velocity, pressure and temperature in the NSRR are similar to the BWR CZP conditions, but much different from those at PWR HZP. The coolant velocity is not expected to markedly influence the fuel dispersal behaviour or the fuel-coolant interaction, but it is reasonable to believe that the higher pressure in the PWR may have a constraining effect on the expulsion of fuel fragments into the water. This assumption follows from the fact that expulsion of solid fuel from high-burnup fuel rods is attributed to gas overpressure.

Moreover, the coolant pressure strongly affects the volume of steam bubbles, generated by the fuel-coolant thermal interaction. From the comparison of specific volumes of saturated steam in table 5.1, it follows that if a certain mass of water is vaporized, the steam volume will be 173 times larger in the NSRR than in the PWR. This striking difference should be accounted for, when evaluating the growth and survival time of steam bubbles, and hence, the risk of pressure wave generation in the coolant.

Water property		**NSRR**	**BWR CZP CRDA**	**PWR HZP REA**
Axial velocity	[ms^{-1}]	0.0	0.7	5.1
Pressure	[MPa]	0.1	0.1	15.5
Temperature	[K]	298	303	565
Saturation temperature	[K]	373	373	618
Subcooling	[K]	75	70	53
Total heat for vaporization	[$J(gH_2O)^{-1}$]	2570	2550	1300
Specific volume of saturated steam	[$m^3(kg)^{-1}$]	1.69	1.69	9.8×10^{-3}

Table 5.1: Coolant conditions in the NSRR, in comparison with those assumed in our analyses of BWR CZP CRDA and PWR HZP REA.

In addition, experiments on melted fuel dispersed into water have shown that the fuel-coolant interaction is affected by the pressure and subcooling of the coolant (Berthoud, 2000). Energetic interaction in the form of vapour explosions is known to become less likely when the coolant pressure increases and the subcooling decreases. In both cases, this is explained by increased stability of the vapour film that encloses the hot fuel fragments. This vapour film serves as a thermal barrier, which hinders fuel-to-coolant heat transfer during the initial phase of fuel dispersion. Since fuel dispersion tests show that the vapour film is more stable under PWR HZP conditions than at room temperature and atmospheric pressure, fuel-coolant interaction is expected to be slower and less energetic in a PWR HZP REA than in the NSRR tests.

Another distinct difference between the cooling conditions at PWR HZP and in the NSRR is the heat needed per unit mass for vaporization of the coolant. Due to the lower subcooling and the higher pressure in the PWR at HZP conditions, only about half the heat is needed for vaporization, in comparison with the NSRR. Considering these differences, we conclude that the fuel-coolant interaction can be much different in a PWR at HZP than in the NSRR. Pulse tests, carried out at typical PWR HZP cooling conditions, are needed to elucidate this issue.

6 Conclusions

Burnup dependent core failure limits for high-burnup light water reactor UO_2 fuel rods subjected to postulated RIAs were assessed by use of best-estimate computational methods. The considered accident scenarios were the PWR HZP REA and the BWR CZP CRDA. The power excursions under these postulated events were in our analyses represented by a Gaussian power pulse, with a fixed width of either 25 ms (HZP REA) or 45 ms (CZP CRDA). These applied power pulses were based on a conservative evaluation of results from three-dimensional core kinetics analyses.

Burnup dependent core failure limits for these two accident scenarios, formulated in terms of threshold enthalpies for incipient fuel pellet melting, were calculated for fuel burnups in the range of 30 to 70 $MWd(kgU)^{-1}$ by use of the FRAPCON-3.2 and SCANAIR-3.2 computer codes. Although differences exist in postulated accident scenarios between the HZP REA and the CZP CRDA considered in our analyses, the calculated core failure limits for these two events are similar. The calculated enthalpy thresholds for melting decrease gradually with fuel burnup, from approximately 960 $J(gUO_2)^{-1}$ at 30 $MWd(kgU)^{-1}$ to 810 $J(gUO_2)^{-1}$ at 70 $MWd(kgU)^{-1}$. The decline is due to depression of the UO_2 melting temperature with increasing burnup, in combination with burnup related changes to the radial power distribution within the fuel pellets.

The postulated HZP REA and CZP CRDA are considered to give the highest energy depositions among conceivable accident scenarios. In addition, these zero power events result in lower enthalpies for pellet melting than RIAs that take place at rated power. Hence, the enthalpy thresholds for fuel incipient melting presented here are lower bounds to RIAs at rated power.

Our calculated failure limits are marginally lower than the limit proposed by the Electric Power Research Institute, USA, for PWR and BWR fuel rods under hot zero power or hot full power RIAs. The agreement is not accidental, since similar methods and assumptions were used in these studies. The difference between the calculated failure limits, approximately 30 $J(gUO_2)^{-1}$, is therefore a good estimate of model-related uncertainties in the performed analyses.

The presented fuel enthalpy thresholds for incipient UO_2 melting provide best-estimate core failure limits for low- and intermediate-burnup fuel. However, pulse reactor tests on high-burnup fuel rods indicate that the accumulation of gaseous fission products within the pellets may lead to fuel dispersal at significantly lower enthalpies than those required for melting, when the fuel burnup exceeds approximately 40 $MWd(kgU)^{-1}$. In order to complete our analyses, a fuel rod failure criterion for this gas-driven dispersal mechanism should be formulated, and corresponding enthalpy thresholds should be calculated for high-burnup fuel rods. This was unfortunately beyond the scope of the present work, and we confined ourselves to a review of experimental data on high-burnup fuel dispersal under RIA.

To date, thirteen pulse reactor tests on high-burnup UO_2 fuel rods have resulted in fuel rod failure.

These rods were all re-fabricated from commercial LWR fuel rods after 4-5 cycles of operation in power reactors, where they had reached final burnups between 44 and 64 $MWd(kgU)^{-1}$. Ten of the failures occurred in the NSRR facility, and extensive clad tube failure and fuel dispersal was observed in at least five of these pulse tests. Three of the failures occurred in the CABRI pulse reactor. These tests were characterized by limited clad tube failure and no or marginal fuel dispersal. The reasons for these very distinct differences in failure behaviour between the NSRR and the CABRI test rods are not clear, but it is assumed that the differences in pulse width, test rod geometry, axial power distribution and coolant conditions between the reactors are important, separately or in combination. In any case, the dissimilar failure behaviour observed in these reactors underlines the importance of prototypical test conditions.

The pulse reactor data on failed high-burnup UO_2 fuel rods show that clad failure does not necessarily lead to fuel pellet dispersal. In other words, the use of a common enthalpy threshold for clad tube failure and fuel dispersal is not particularly well supported by experiments. In fact, the data suggest that a peak fuel enthalpy of at least 500 $J(gUO_2)^{-1}$ is required to expel a significant part (>10 %) of the fuel inventory into the coolant. However, this empirical enthalpy threshold for fuel dispersal from high-burnup fuel rods cannot be directly applied to light water reactors, since the power pulses and/or the cooling conditions used in the pulse tests differ notably from those expected in LWRs under RIA. This reservation pertains in particular to PWR hot reactor cooling conditions, for which experimental data on fuel dispersal, fuel-coolant interaction and energy conversion ratios are lacking.

7 References

Adamson, M.G., Aitken, E.A. and Caputi, R.W., 1985.
Experimental and thermodynamic evaluation of the melting behavior of irradiated oxide fuels, J. Nucl. Mat. 130, pp 349-365.

Berna, G.A., Beyer, C.E., Davis, K.L. and Lanning, D.D., 1997.
FRAPCON-3: A computer code for the calculation of steady-state, thermal-mechanical behavior of oxide fuel rods for high burnup,
NUREG Report NUREG/CR-6534, Volume 2 (1997).

Berthoud, G., 2000.
Vapor explosions, Annular Review of Fluid Mechanics 32, pp 573-611.

Christensen, J.A., Allio, R.J. and Biancheria, A., 1964.
Melting point of irradiated uranium dioxide,
Transactions of the American Nuclear Society, 7(2), pp 390-391.

Carbajo, J.J., Yoder, G.L., Popov, S.G. and Ivanov, V.K., 2001.
A review of the thermophysical properties of MOX and UO2 fuels,
J. Nucl. Mat. 299, pp 181-198.

Cook, B.A. and Martinson, Z.R., 1984.
Reactivity initiated accident test series, test RIA 1-4 fuel behavior report,
NUREG Report NUREG/CR-3938, September 1984.

Corradini, M.L., Kim, B.J. and Oh, M.D., 1988.
Vapor explosions in light water reactors: A review of theory and modelling,
Progress in Nuclear Energy, 22(1), pp 1-117.

Cunningham, M., Beyer, C.E., Medvedev, P.G. and Berna, G.A., 2001.
FRAPTRAN: A computer code for the transient analysis of oxide fuel rods,
NUREG Report NUREG/CR-6739, Volume 1, August 2001.

Federici, E., Lamare, F., Bessiron, V. and Papin, J., 2000.
Status of development of the SCANAIR code for the description of fuel behavior under reactivity initiated accidents, Proc. of the 2000 Int. Topical Meeting on LWR Fuel Performance, Park City, Utah, USA, April 10-13, 2000.

Fink, J.M., 1996.
Melting point of uranium dioxide, INSC Material Properties Database,
International Nuclear Safety Center (INSC), Argonne National Laboratory, USA.
Available via the internet at www.insc.anl.gov/matprop.

Fuketa, T., Mori, Y., Sasajima, H., Ishijima, K. and Fujishiro, T., 1995.
Behavior of high burnup PWR fuel under a simulated RIA condition in the NSRR,
Proc. of the CSNI specialist meeting, Cadarache, France, September 12-14, 1995.
Report NEA/CSNI/R(95)22, OECD Nuclear Energy Agency.

Fuketa, T., Sasajima, H., Mori, Y. and Ishijima, K., 1997.
Fuel failure and fission gas release in high burnup PWR fuels under RIA conditions,
J. Nucl. Mat. 248, pp 249-256.

Fuketa, T., Nakamura, T., Sasajima, H., Nagase, F., Uetsuka, H., Kikuchi. K. and Abe, T., 2000.
Behavior of PWR and BWR fuels during reactivity-initiated accident conditions,
Proc. ANS Topical Meeting on Light Water Reactor Fuel Performance, Park City, Utah, April 10-13, 2000.

Fuketa, T., Sasajima, H. and Sugiyama, T., 2001.
Behavior of high-burnup PWR fuels with low-tin Zircaloy-4 cladding under reactivity-initiated-accident conditions, Nucl. Technology, 133, pp 50-62.

Gabrielson, P., 2004.
Effektpulskaraktäristik vid RIA för PWR, (In Swedish),
Vattenfall Bränsle Report PB-236/03, January 2004.

Glasstone, S. and Sesonske, A., 1991.
Nuclear reactor engineering, 3rd ed.,
Krieger Publishing Company, Malabar, Florida, USA.

Harding, J.H. and Martin, D.G., 1989.
A recommendation for the thermal conductivity of UO_2,
J. Nucl. Mat. 166, pp 223-226.

IAEA, 2001.
Thermohydraulic relationships for advanced water cooled reactors,
Report IAEA-TECDOC-1203, International Atomic Energy Agency, Vienna, Austria.

In de Betou, J., Jernkvist, L.O., Massih, A.R., Rudling, P., Rönnberg, G., Stepniewski, M. and Wiksell, G., 2004. *Assessment of burnup-dependent fuel rod failure threshold under reactivity-initiated accidents in light water reactors*,
Proc. of the 2004 Int. Meeting on LWR Fuel Performance, Orlando, Florida, USA, September 19-22, 2004.

Ishijima, K., Mori, Y., Fuketa, T. and Sasajima, H., 1995.
Postulated mechanisms on the failure of 50 MWd/kgU PWR fuel in the NSRR experiment and the related research programs in JAERI,
Proc. of the CSNI specialist meeting, Cadarache, France, September 12-14, 1995.
Report NEA/CSNI/R(95)22, OECD Nuclear Energy Agency.

Jernkvist, L.O., 2002.
FRAPAIR: An interface program between FRAPCON-3 and SCANAIR 3.2,
Quantum Technologies Report TR 02-003, Uppsala, Sweden.

Jernkvist, L.O. and Massih, A.R., 2002.
Analysis of the effect of UO_2 *high burnup microstructure on fission gas release*,
Swedish Nuclear Power Inspectorate (SKI) Research Report 02:56, Stockholm, Sweden.

Jernkvist, L.O. and Massih, A.R., 2004.
Assessment of fuel rod failure thresholds for reactivity initiated accidents, Swedish Nuclear Power Inspectorate (SKI) Research Report 2004:33, Stockholm, Sweden.

Komatsu, J, Tachibana, T. and Konashi, K., 1988.
The melting temperature of irradiated oxide fuel,
J. Nucl. Mat. 154, pp 38-44.

Lamare, F., 2001.
The SCANAIR code version 3.2: Reference documentation,
Note Technique SEMAR 01/37, Nuclear Protection and Safety Institute (IPSN), France.

Lamare, F. and Latche, J.C., 1995.
SCANAIR: A computer code for reactivity initiated accidents in LWRs,
Note Technique SEMAR 95/01, Nuclear Protection and Safety Institute (IPSN), France.

Lanning, D.D., Beyer, C.E. and Berna, G.A., 1997.
FRAPCON-3: Integral assessment,
NUREG Report NUREG/CR-6534, Volume 3 (1997).

Lemoine, F., 1997.
High burnup fuel behavior related to fission gas effects under reactivity initiated accidents (RIA) conditions, J. Nucl. Mat. 248, pp 238-248.

Lespiaux, D., Noirot, J. and Menut, P., 1997.
Post-test examinations of high burnup PWR fuels submitted to RIA transients in the CABRI facility, Proc. ANS Topical Meeting on Light Water Reactor Fuel Performance, Portland, Oregon, March 2-6, 1997, pp 650-658.

Lucuta, P.G., Matzke, Hj. and Verall, R.A., 1994.
Modelling of UO_2 based SIMFUEL thermal conductivity: The effect of the burnup,
J. Nucl. Mat. 217, pp 279-286.

MacDonald, P.E., Seiffert, S.L., Martinson, Z.R., McCardell, R.K., Owen, D.E. and Fukuda, S.K., 1980. *Assessment of light-water reactor fuel damage during a reactivity-initiated accident*, Nucl. Safety 21(5), pp 582-602.

Maeder, C. and Wand, H., 2004.
Sicherheitskriterien für Reaktivitätsstörfälle in Schweizerischen Kernkraftwerken,
(In German), Report HSK-AN-5208, Swiss Federal Nuclear Safety Inspectorate (HSK), Villigen, Switzerland.

Manzel, R. and Walker, C.T., 2000.
High burnup fuel microstructure and its effect on fuel rod performance,
Proc. of the 2000 Int. Topical Meeting on LWR Fuel Performance, Park City, Utah, USA, April 10-13, 2000.

Manzel, R. and Walker, C.T., 2002.
EPMA and SEM of fuel samples from PWR fuel rods with an average burn-up of around 100 MWd/kgHM,
J. Nucl. Mat. 301, pp 170-182.

Nakamura, T., Kusagaya, K. and Fuketa, T., 2002a.
High-burnup BWR fuel behavior under simulated reactivity-initiated accident conditions, Nucl. Technology, 138, pp 246-259.

Nakamura, T., Sasajima, H., Yoshinaga, M. and Kusagaya, K., 2002b.
NSRR RIA tests on PWR, BWR and MOX fuels,
Proc. Fuel Safety Research Specialist's Meeting, Tokai, Japan, March 4-5, 2002.

Nakamura, T., Fuketa, T., Sugiyama, T. and Sasajima, H., 2004.
Failure thresholds of high burnup BWR fuel rods under RIA conditions,
J. Nucl. Sci. Techn. 41(1), pp 37-43.

NUREG-0800, 1981.
Standard review plan for the review of safety analysis reports for nuclear power plants, LWR edition, section 4.2: Fuel system design, U.S. Nuclear Regulatory Commission report NUREG-0800, Rev. 2, Washington D.C.

Papin, J., Cazalis, B., Frizonnet, J.M., Federici, E. and Lemoine, F., 2003.
Synthesis of CABRI-RIA tests interpretation,
Proc. Eurosafe Conference, Paris, November 25-26, 2003.

Popov, S.G., Carbajo, J.J., Ivanov, V.K. and Yoder, G.L., 2000.
Thermophysical properties of MOX and UO_2 fuels including the effects of irradiation,
Oak Ridge National Laboratory report ORNL/TM-2000/351,
Oak Ridge, TN, USA, November 2000.

RG-1.77, 1974.
Regulatory Guide 1.77 – Assumptions used for evaluating a control rod ejection accident for pressurized water reactors,
US Atomic Energy Commission, 1974.

Ronchi, C., Scheindlin, M., Musella, M. and Hyland, G.J., 1999.
Thermal conductivity of uranium dioxide up to 2900 K from simultaneous measurements of the heat capacity and thermal diffusivity,
J. Applied Physics, 81(2), pp 776-789.

SKI, 1995.
Ändrade gränser för härd- och kapslingsskada vid analys av reaktivitetsolyckor,
(In Swedish), SKI Beslut 5.66-941618, Swedish Nuclear Power Inspectorate (SKI), January 18, 1995.

Sugiyama, T. and Fuketa, T., 2000.
Mechanical energy generation during high burnup fuel failure under reactivity initiated accident conditions, J. Nucl. Sci. Techn. 37(10), pp 877-886.

Sugiyama, T., Fuketa, T., Ozawa, M. and Nagase, F., 2004.
RIA-simulating experiments on high burnup PWR fuel rods with advanced cladding alloys, Proc. of the 2004 Int. Meeting on LWR Fuel Performance, Orlando, Florida, USA, September 19-22, 2004.

Tsuruta, T., Ochiai, M. and Saito, S., 1985.
Fuel fragmentation and mechanical energy conversion ratio at rapid deposition of high energy in LWR fuels, J. Nucl. Sci. Techn. 22(9), pp 742-754.

Waeckel, N., Bernaudat, C. and Salles, B., 2000.
EDF proposed safety domain for rod ejection accidents in a PWR,
Proc. ANS Topical Meeting on Light Water Reactor Fuel Performance, Park City, Utah, April 10-13, 2000.

Wiksell, G., 2003.
Pulsbredder vid transienter beräknade med S3K, (In Swedish),
OKG Report 2003-08073.

Yang, R., Montgomery, R.O. and Waeckel, N., 2003.
Revised reactivity initiated accident acceptance criteria for high burnup fuel,
Proc. European Nuclear Society ENS TopFuel 2003 Conference, Wurzburg, Germany, March 16-19, 2003.

Appendix A: Current core failure limit for RIA in Sweden

The current core failure limit for reactivity initiated accidents in Sweden was defined by the Swedish Nuclear Power Inspectorate (SKI) in the beginning of 1995 (SKI, 1995). The core failure limit, which is applicable to RIA in both BWRs and PWRs, is defined in terms of maximum allowable radial average fuel pellet enthalpy [cal(gUO_2)$^{-1}$] with respect to fuel pellet radial average burnup in [MWd($kgUO_2$)$^{-1}$], as shown in table A.1. For convenience, the limit is also transformed to units applied throughout this report. Figure A.1 shows the core failure limit.

Fuel pellet radial average burnup [MWd($kgUO_2$)$^{-1}$]	**Fuel pellet radial average enthalpy [cal(gUO_2)$^{-1}$]**	**Fuel pellet radial average burnup [MWd(kgU)$^{-1}$],**	**Fuel pellet radial average burnup [J(gUO_2)$^{-1}$]**
0	230	0.0	963
33	230	37.4	963
40	100	45.4	419
50	60	56.7	251
60	30	68.0	126

Table A.1: Current core failure limit applied in Sweden for RIA.

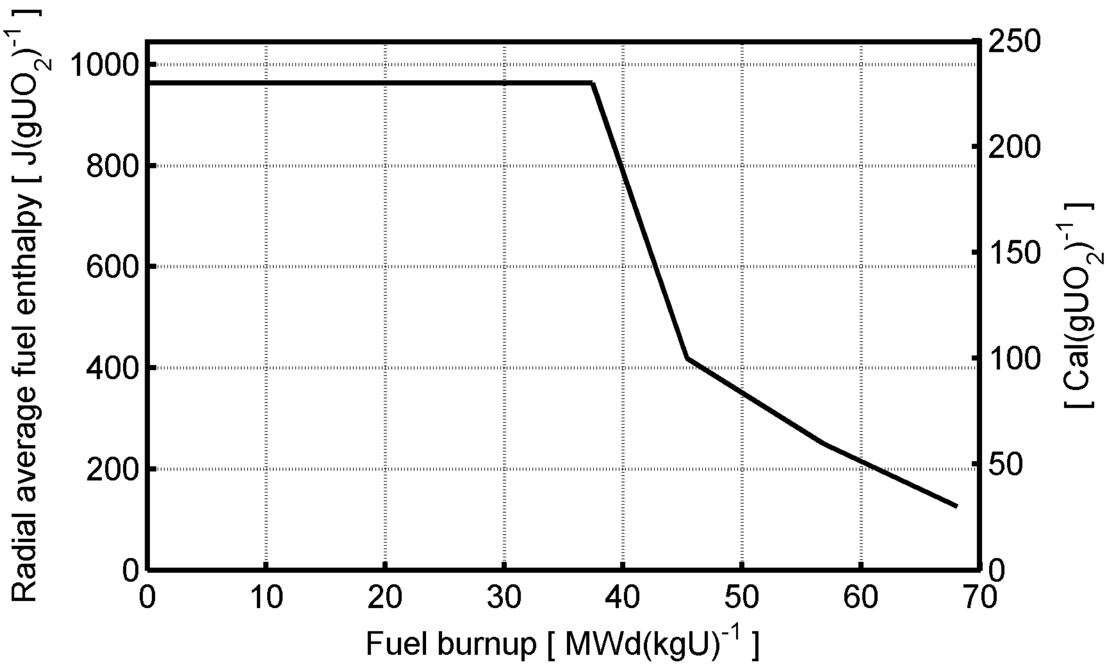

Figure A.1: Current core failure limit applied in Sweden for RIA.

Appendix B: Failed fuel rods in pulse reactor tests

This appendix contains a review of RIA simulation tests, performed in three different pulse reactors on pre-irradiated light water reactor UO_2 fuel rods, which have resulted in fuel rod failure. Particular emphasis is given to the observed mode of clad tube failure and the measured extent of fuel pellet dispersion into the coolant. Two of the tests were performed in the Special Power Excursion Reactor (SPERT), USA. Three tests were made in the French CABRI pulse reactor, and 17 tests were carried out in the Japanese Nuclear Safety Research Reactor (NSRR). The reactor conditions, as well as the investigated test rods, differ significantly between these studies. This is illustrated in table B.1, which summarizes test conditions and key fuel rod properties in each experimental program.

Facility	**SPERT**	**NSRR**	**CABRI**
Reactor conditions			
Coolant medium	Stagnant water	Stagnant water	Flowing sodium
Coolant temperature [K]	293	298 - 358	553
Coolant pressure [MPa]	0.1	0.1	0.5
Power pulse width [ms]	16 – 17	4 – 7	9 - 75
Failed fuel rods in tests			
Number of failed fuel rods (PWR/BWR/JMTR)	2 (0/2/0)	17 (5/5/7)	3 (3/0/0)
Burnup [$MWd(kgU)^{-1}$]	31.8 - 32.7	21 – 61	60 – 64
Clad oxide thickness [µm]	≈ 65	2 – 60	60 – 130
Rod active length [mm]	132	122 – 135	440 – 550
Peak fuel enthalpy [$J(gUO_2)^{-1}$] ($cal(gUO_2)^{-1}$)	600 – 645 (143 – 154)	306 – 910 (73 – 217)	410 – 475 (98 – 113)
Failure enthalpy [$J(gUO_2)^{-1}$] ($cal(gUO_2)^{-1}$)	356 – 600 (85 – 143)	251 – 850 (60 – 203)	117 – 339 (28 – 81)

Table B.1: Overview of pulse reactor tests on pre-irradiated UO_2 fuel rods, which have resulted in rod failure. The peak- and failure enthalpies are axial peak, radial average values for the fuel pellet column.

B.1 Failed BWR fuel rods

Most of the BWR-type fuel rods that failed in the SPERT were only marginally irradiated, but two of the failed rods were pre-irradiated to about 32 $MWd(kgU)^{-1}$ in the Engineering Test Reactor (ETR) at very high linear heat generation rates, 46-67 kWm^{-1}, resulting in fuel high-temperature restructuring and formation of central holes in the fuel pellets (MacDonald et al., 1980).

Hence, the pre-irradiation conditions were not typical for those in a commercial BWR. Moreover, the fuel rod design differed significantly from typical BWR fuel: The UO_2 fuel pellets were enriched with 7 % ^{235}U, and the outer diameter of the clad tube was 7.95 mm. The small-diameter rods, in literature denoted GEX, were designed to increase the attainable energy deposition in the RIA simulation facility, and their clad wall thickness and fuel-cladding gap were reduced proportionally to the clad diameter. The design and testing conditions for the two pre-irradiated rods that failed in the SPERT, CDC-756 and CDC-859, are given in table B.2.

The rod CDC-756 failed by one small axial split in the clad tube, without any dispersal of fuel into the coolant. For the rod CDC-859, a very small amount of fuel was dispersed, as the clad tube failed by three long axial splits of brittle nature. In addition, a small axial split through a hydride blister was observed in rod CDC-859 (MacDonald et al., 1980).

Parameter	**Failed BWR fuel rods**						
	CDC-756	CDC-859	FK-6	FK-7	FK-9	FK-10	FK-12
Fuel design	GEX	GEX	8×8	8×8	8×8	8×8	8×8
Clad material	Std Zr-2	Std Zr-2	Std Zr-2 Zr-liner	Std Zr-2 Zr-liner	Std Zr-2 Zr-liner	Std Zr-2 Zr-liner	Std Zr-2 Zr-liner
Test reactor	SPERT	SPERT	NSRR	NSRR	NSRR	NSRR	NSRR
Fuel burnup [$MWd(kgU)^{-1}$]	32.7	31.8	61	61	61	61	61
Fuel enrichment [%]	7.0	7.0	4.5	4.5	4.5	4.5	4.5
Pulse width [ms]	17	16	4.3	4.3	5.7	5.2	5.5
Coolant temperature [K]	293	293	298	298	298	353	358
Coolant pressure [MPa]	0.1	0.1	0.1	0.1	0.1	0.1	0.1
Clad oxide thickness [μm]	≈65	≈65	≈30	≈30	≈30	<27	<27
Peak fuel enthalpy [$J(gUO_2)^{-1}$]	600	645	548	540	377	430	373
Fuel enthalpy at clad failure [$J(gUO_2)^{-1}$]	≈600	356	293	260	360	335	301
Fuel pellet loss [wt%]	0	Very little	99	99	99	*	*
Type of clad tube failure	Small AS	Three AS	AS CB	AS CB	AS CB[2]	AS	AS CB

Table B.2: Key data for failed BWR fuel rods. An asterisk (*) is used in all entries, for which information is unavailable. AS: Axial split. CB: Circumferential break.

[2] Atypical circumferential break at the weld to the bottom end fitting of the sample, leading to large fuel pellet loss (Nakamura et al., 2002a).

Five tests performed in the NSRR on rodlets, which were re-fabricated from full-length BWR fuel rods after 5 cycles of operation in unit 2 of the Fukushima-Daichi power plant, Japan, have resulted in rod failure. All the failed rods belonged to the FK-series of tests. The peak LHGR under the pre-irradiation was about 35 kWm^{-1}, and fission gas release at end of the pre-irradiation was reported to be 12-14 %. The design and testing conditions are given for each of the rods in table B.2. The data are compiled from the works of Nakamura et al. (2002a) and (2004).

The clad tubes of the failed rods FK-6 and FK-7 were broken apart into three pieces, and almost all of the fuel material was recovered as fine fragments in the coolant water after the tests. The average size of the fuel fragments was 43 and 56 μm for FK-6 and FK-7, respectively.

Rod FK-9 failed through a long axial split in the clad tube, which developed into a complete circumferential break at the bottom end fitting (Nakamura et al., 2002a; 2002b). Since the end fitting was separated from the rest of the rod, nearly all of the fuel was lost through this break. The average size of the fuel fragments recovered from the coolant water was 81 μm. This mode of failure, as shown in figure B.1, must be considered as atypical, since the circumferential break occurred in the weld to the end fitting and in the heat affected zone at the weld. The complete separation of the end fitting from the rod resulted in a nearly complete (99 %) dispersal of the fuel inventory into the coolant. The fuel pellet loss for FK-9 would probably have been much less, had the rod not failed in this atypical manner. It should be remarked, that the same type of weld-related failure has been reported for two other NSRR tests, carried out on the PWR rods HBO-1 and OI-11, as discussed in section B.2.

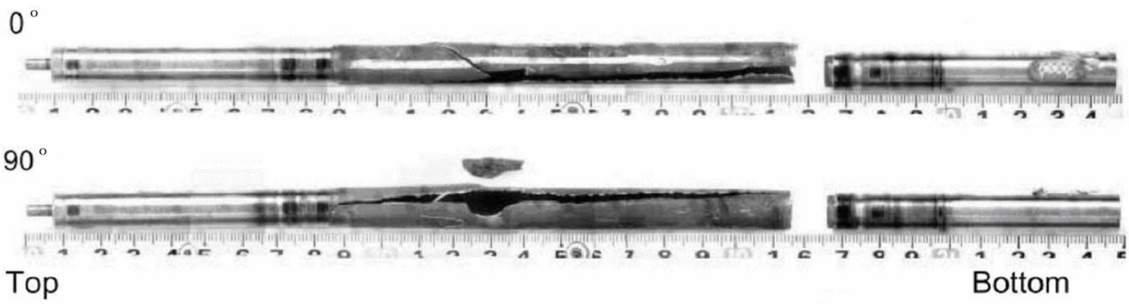

Figure B.1: Post-test appearance of rod FK-9 (Nakamura et al., 2002b).

The two rods FK-10 and FK-12 were tested at somewhat higher coolant temperatures than normally used in the NSRR. However, the elevated temperature does not seem to have any significant effect on the failure mode. Rod FK-10 failed through an axial split of the cladding, and a small piece of the clad tube was separated from the rest of the rod (Nakamura et al., 2002b). Rod FK-12 failed through a long axial split and a circumferential break of the clad tube (Nakamura et al., 2004). The circumferential break was located in the middle of the active part of the rod. The fuel pellet loss has not yet been reported for FK-10 and FK-12, but from post-test appearance of these rods, it is clear that a significant part of the fuel inventory must have been dispersed into the coolant.

B.2 Failed PWR fuel rods

Three tests performed on pre-irradiated PWR fuel rods in the CABRI reactor and five tests in the NSRR have resulted in rod failures. All tests were made on rodlets, which were re-fabricated from full-length PWR rods after pre-irradiation in commercial power reactors. The rods that failed in CABRI were pre-irradiated in the Gravelines power plant, France, to burnups in the range of 60 to 64 $MWd(kgU)^{-1}$. These rods had standard Zircaloy-4 cladding, which was severely corroded, with spalled oxide and non-uniform hydride distribution. The test conditions for these rods are summarized in table B.3, where the presented data are taken from the paper by Papin et al. (2003).

The PWR fuel rods that failed in RIA simulation tests in the NSRR belong to three different test series. The rods HBO-1 and HBO-5 were pre-irradiated in Ohi-1 for four cycles, as reported by Fuketa et al. (1995), (1997) and (2001). The rod average LHGR in these four cycles was about 16 kWm^{-1}, and about 15 kWm^{-1} for the last cycle. These fuel rods had standard Zircaloy-4 cladding (1.5 wt% Sn) and fuel pellets with fairly low enrichment. The rods TK-2 and TK-7 had low-tin (1.3 wt% Sn) Zircaloy-4 cladding, and were pre-irradiated in Takahama-3, (Fuketa et al., 2001) and (Sugiyama & Fuketa, 2000). Finally, rod OI-11 had ZIRLO cladding, and was pre-irradiated for four cycles in Ohi-4 (Sugiyama et al., 2004).

The rods tested in CABRI differ markedly from those tested in NSRR, with respect to both fuel dispersal and post-test appearance of the failed cladding. The rods tested in CABRI show no or marginal fuel dispersal, since the clad tubes failed by narrow axial splits. These splits, which were typically 50-100 mm long, were found close to the peak power axial position of the fuel rod (Waeckel et al., 2000). The rods tested in the NSRR, on the other hand, failed by wider axial splits, which usually extended over the entire active length of the sample. In many cases, the paths of these splits passed through the heat affected zone close to thermocouples that were welded to the clad tube surface. In addition, circumferential breaks occurred in some of the NSRR rods, in contrast to CABRI. Consequently, the fractional loss of fuel material was generally larger for the NSRR rods than for those tested in CABRI.

The failure mode of rod HBO-1 has been discussed in detail by Ishijima et al. (1995). In summary, post-test examinations of HBO-1 revealed three long axial splits of the cladding tube. One of these splits extended to the weld at the top end fitting, and continued circumferentially along the weld. This crack did not develop into a complete circumferential break. However, another of the axial splits extended to the weld of the bottom end fitting, and resulted in separation of the bottom end fitting from the rest of the rod. On-line measurements of fuel stack elongation under the test indicated that the fuel column was expelled mainly through this circumferential break at the bottom end, rather than through the clad axial splits. Hence, the large fuel pellet loss (67 %) for HBO-1 is most likely a consequence of the atypical failure mode in this test.

Large bending of the rod was observed for HBO-1, which together with oval deformation of the clad tube suggests that the rod was axially constrained during the test. Although the axial constraint is unlikely to have had any major effect on the initiation of clad failure, it probably enlarged the openings of the axial splits and made them extend along the welds at the top and bottom end fittings. Also rod OI-11 failed completely through a circumferential break along the weld to the bottom end fitting, see figure B.2. The separation of the bottom end fitting explains the complete dispersal of fuel in this test (Sugiyama et al., 2004).

The remaining PWR NSRR rods in table B.3 failed through axial splits, leading to moderate fuel dispersal into the coolant. The failures of these rods have been analysed by Sugiyama and Fuketa (2000), Sugiyama et al. (2004), and also by Fuketa et al. (1997), (2000) and (2001).

	Failed PWR fuel rods							
Parameter	Na-1	Na-8	Na-10	HBO-1	HBO-5	TK-2	TK-7	OI-11
Fuel design	17×17	17×17	17×17	17×17	17×17	17×17	17×17	17×17
Clad material	Std Zr-4	Std Zr-4	Std Zr-4	Std Zr-4	Std Zr-4	Low-tin Zr-4	Low-tin Zr-4	ZIRLO
Test reactor	CABRI	CABRI	CABRI	NSRR	NSRR	NSRR	NSRR	NSRR
Fuel burnup [$MWd(kgU)^{-1}$]	64	60	63	50	44	48	50	58
Fuel enrichment [%]	4.5	4.5	4.5	3.2	3.2	4.1	4.1	4.5
Pulse width [ms]	9.5	75	31	4.4	4.4	4.3	4.4	4.4
Coolant temperature [K]	553	553	553	298	298	298	298	298
Coolant pressure [MPa]	0.5	0.5	0.5	0.1	0.1	0.1	0.1	0.1
Clad oxide thickness [μm]	80-100 Spalled	84-126 Spalled	60-100 Spalled	43	60	35	30	28
Peak fuel enthalpy [$J(gUO_2)^{-1}$]	475	410	410	306	334	450	398	657
Fuel enthalpy at clad failure [$J(gUO_2)^{-1}$]	117-151	327	339	250	320	250	360	502
Fuel pellet loss [wt%]	2	0	0	67	5	7	Little	100
Type of clad tube failure	AS	AS	AS	AS CB[3]	AS	AS	AS	AS CB[3]

Table B.3: Key data for failed PWR fuel rods.
AS: Axial split. CB: Circumferential break.

[3] Atypical circumferential break at the weld to the bottom end fitting of the sample, leading to large fuel pellet loss; see the works of (Ishijima et al., 1995) and (Sugiyama et al., 2004).

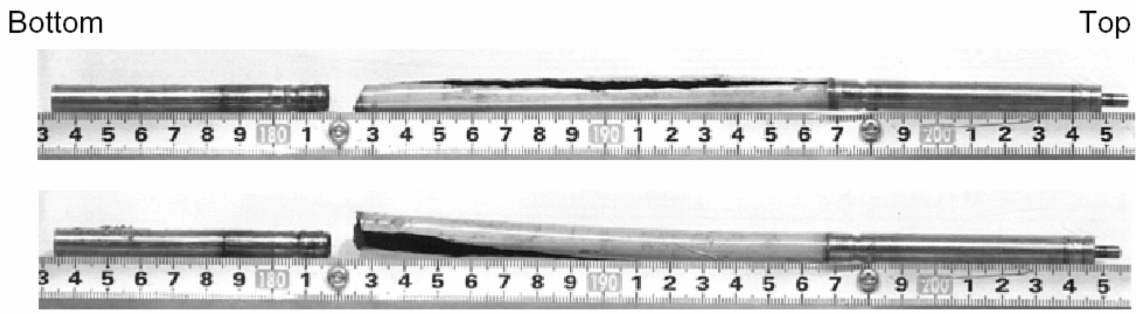

Figure B.2: Post-test appearance of rod OI-11 (Sugiyama et al., 2004).

B.3 Failed JMTR fuel rods

To date, a total of 22 short-length rodlets that have been pre-irradiated in the Japanese Material Test Reactor (JMTR) have undergone RIA simulation tests in the NSRR. Seven of the samples failed, and key data for these rods, compiled from the works of Fuketa et al. (1997) and Sugiyama and Fuketa (2000), are summarized in table B.4.

	Failed JMTR fuel rods						
Parameter	JM-4	JM-5	JM-12	JM-14	JMN-1	JMH-3	JMH-5
Fuel design	14×14	14×14	14×14	14×14	14×14	14×14	14×14
Clad material	Std Zr-4	Std Zr-4	Std Zr-4	Std Zr-4	Std Zr-4	Std Zr-4	Std Zr-4
Test reactor	NSRR	NSRR	NSRR	NSRR	NSRR	NSRR	NSRR
Fuel burnup [$MWd(kgU)^{-1}$]	21	26	38	38	22	30	30
Fuel enrichment [%]	10	10	10	10	10	20	20
Pulse width [ms]	5.5	5.6	5.3	6.0	7.1	6.2	6.2
Coolant temperature [K]	298	298	298	298	298	298	298
Coolant pressure [MPa]	0.1	0.1	0.1	0.1	0.1	0.1	0.1
Clad oxide thickness [μm]	<2	<2	<2	<2	<2	<2	<2
Peak fuel enthalpy [$J(gUO_2)^{-1}$]	743	697	754	670	628	850	910
Fuel enthalpy at clad failure [$J(gUO_2)^{-1}$]	743	697	653	515	486	850	790
Fuel pellet loss [wt%]	0	0	0	Very little	0	Yes	20
Type of clad tube failure	Small AS	Small AS	*	AS	*	AS	*

Table B.4: Key data for failed JMTR fuel rods. An asterisk (*) is used in all entries, for which information is unavailable. AS: Axial split.

The JMTR rods are of 14×14 PWR type, with standard Zircaloy-4 cladding, but the fuel enrichment is significantly higher than in commercial PWR fuel: 10 % in the JM and JMN test series, and 20 % in the JMH test rods. The high enrichment of ^{235}U in the JMTR fuel, which should be compared to the 3-5 % enrichment used in commercial PWR rods, allows for higher energy depositions during the tests. Unfortunately, it also affects the radial power distribution within the fuel pellets. Due to the high fuel enrichment and the fact that pre-irradiation took place at high LHGR (25-35 kWm^{-1}) in an un-pressurized, non-oxidizing helium environment, the JMTR test rods are not representative of LWR fuel.

Most of the failed test rods in table B.4 had hydride blisters or hydride clusters in the cladding after pre-irradiation in the JMTR. As discussed by Fuketa and co-workers, these hydride accumulations played an important role in the failure of the rods, Fuketa et al. (1995) and (1997). Small through-wall cracks in the vicinity of several hydride clusters were found in rods JM-4 and JM-5, and long axial splits, emanating from hydride clusters, were found in rods JM-14, JMH-3 and JMH-5.

Significant fuel dispersal was reported for JMH-3 and JMH-5, which are the rods subjected to the highest fuel enthalpies among all JMTR rods tested in the NSRR.

B.4 Summary of rod failures in pulse reactor tests

The pulse test data from sections B.1 to B.3 are summarized in figure B.3, which shows the measured fuel dispersion from 20 UO_2 fuel rods that have failed under RIA simulation tests in the SPERT, CABRI and the NSRR. Filled symbols represent samples, for which more than 10 % of the UO_2 fuel inventory was dispersed into the coolant under the test, whereas open symbols are samples with no or marginal fuel loss.

From figure B.3, it is clear that significant fuel dispersal was observed in only two out of nine fuel rods within the low- and intermediate burnup range, which is here defined by the SPERT and JMTR test rods, ranging in burnup from 21 to 38 $MWd(kgU)^{-1}$. Moreover, the peak radial average fuel enthalpies in these two rods were very high, 850 and 910 $J(gUO_2)^{-1}$, respectively. Hence, according to these tests, the potential for dispersion of non-molten fuel fragments from failed fuel rods is low at low- and intermediate fuel burnup.

The situation is much different at high burnup. Considering the failed rods in the upper burnup range of figure B.3, i.e. in the range of 44 to 64 $MWd(kgU)^{-1}$, we find that significant fuel dispersal was reported in five of the eleven tests. A common feature of these five tests is that the clad tubes failed by circumferential breaks. However, we should remember that the large fuel dispersal in three of the rods, HBO-1, FK-9 and OI-11, is a consequence of atypical clad tube failure. In these samples, the fuel column was dispersed through a circumferential break along the weld to the bottom end fitting, which was completely separated from the upper part of the rod. This failure mode is not transferable to full length fuel rods, for which only a minor part of the fuel column could possibly be expelled through a break at the bottom end plug.

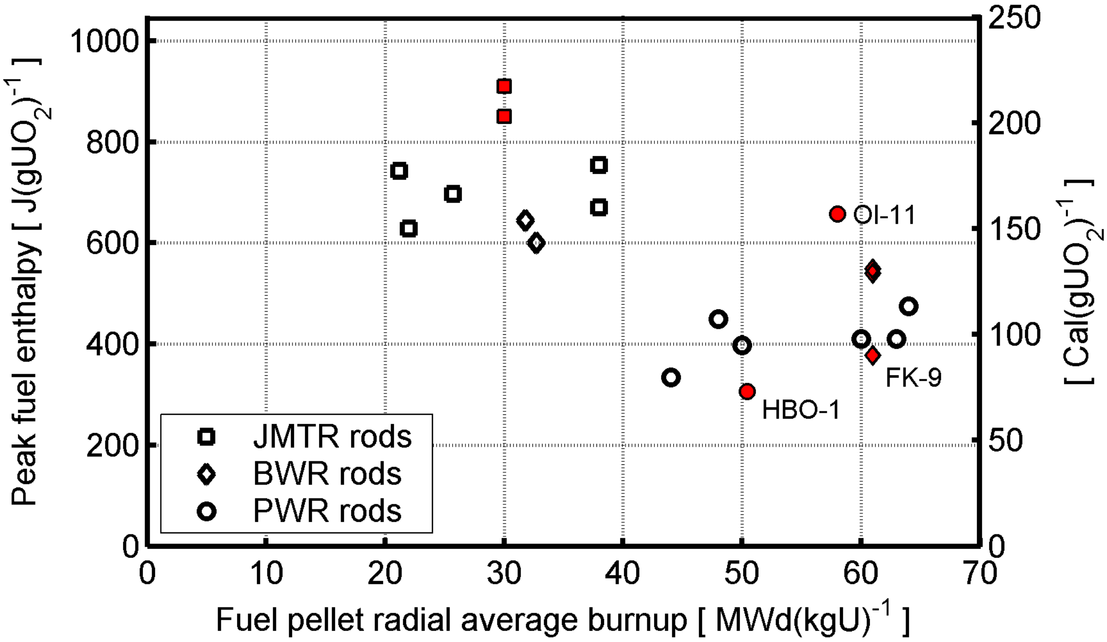

Figure B.3: Fuel dispersal observed for 20 pre-irradiated fuel rods, all of which have failed under pulse reactor tests. Filled symbols represent samples, for which more than 10 % of the UO_2 fuel inventory was dispersed into the coolant under the test, whereas open symbols are samples with no or marginal fuel loss.

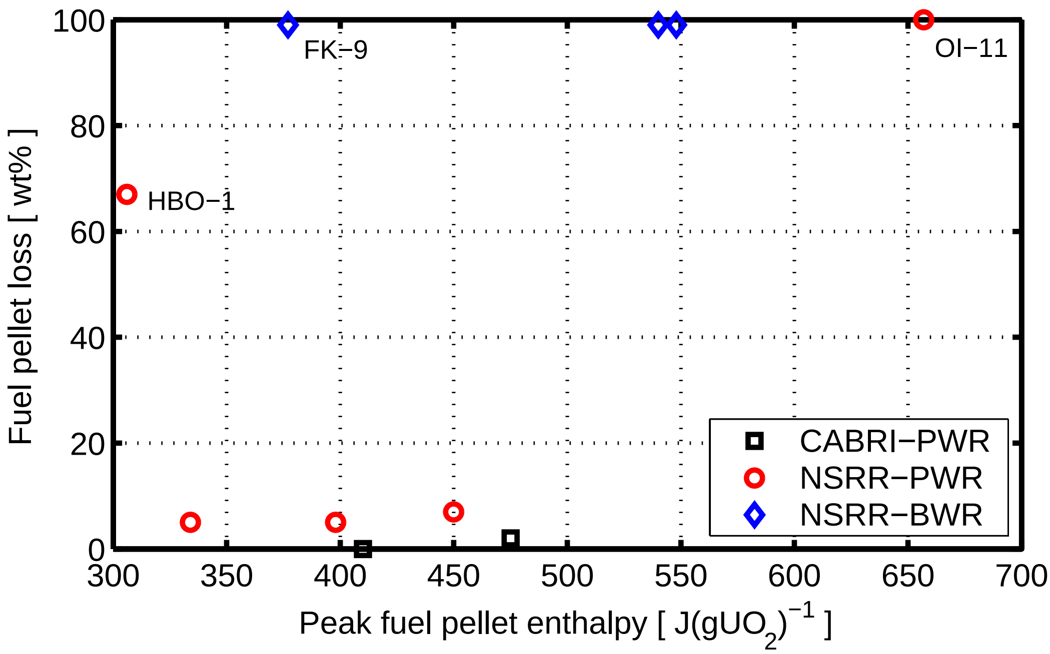

Figure B.4: Measured fuel loss in the failed BWR and PWR high-burnup fuel rods shown in figure B.3. The fuel burnup of these rods ranges from 44 to 64 MWd(kgU)$^{-1}$. The rods HBO-1, FK-9 and OI-11 failed in the weld to the bottom end fitting, i.e. in an atypical mode of clad tube failure.

The outcome of these eleven high-burnup tests is also shown in figure B.4, where the degree of fuel loss is plotted with respect to peak fuel enthalpy under the test. Except for the non-representative tests HBO-1 and FK-9, only a minor portion of the fuel inventory was dispersed into the coolant for tests performed at peak fuel enthalpies below 500 $J(gUO_2)^{-1}$. The data in figure B.4 thus suggest that a peak fuel enthalpy of at least 500 $J(gUO_2)^{-1}$ is required to expel a significant part of the fuel inventory from the high-burnup UO_2 fuel rods in these tests.

As already mentioned, there are large differences in failure behaviour between the rods tested in the NSRR and the CABRI pulse reactor, respectively. In the NSRR, the rods failed primarily by axial or spiral splits in the clad tube. These splits had wide openings, and they usually extended over the entire active length of the rod. Some of the rods were also broken apart by circumferential cracks, resulting in large loss of fuel. The three rods in CABRI all failed by multiple axial splits in the clad tube. The splits were typically 50-100 mm long, with narrow openings, and they were concentrated to the central peak power region of the test rods. Marginal fuel loss, 2 % of the inventory, was observed for rod Na-1, but no fuel was dispersed in the other two tests in CABRI.

The reasons to the observed differences in failure behaviour between the NSRR and the CABRI test rods are not clear, but they are most likely related to the differences in pulse width, test rod geometry and coolant conditions between the reactors; see table B.1.

The pulse width affects the rate of mechanical loading imposed on the cladding tube from the pellet-clad mechanical interaction, and more importantly, a wider pulse allows more time for heat-up of the clad tube under the RIA. The large and brittle cladding cracks observed in the NSRR rods are consistent with the short power pulses (≈5 ms) used in this facility. Not only the clad tube failure behaviour is affected by pulse width, but also the fuel pellet fragmentation. For the narrow pulses used in the NSRR, fuel heat conduction under the energy deposition is negligible. This leads to high local temperatures and steep temperature gradients at the fuel pellet periphery, which promotes grain boundary de-cohesion and fuel fragmentation. A wide power pulse, on the other hand, allows some heat conduction, both within the fuel pellet and from the pellet to the clad tube. This leads to a more uniform temperature distribution within the pellet and thus to a lower potential for fuel fragmentation. In addition, a wide power pulse may allow intergranular gas bubbles to gradually de-pressurize, by venting of their gas into the rod plenum volume.

The active length of the rods tested in CABRI is about 500 mm, and the rods are subjected to a non-uniform axial power distribution under the pulse test. There is a considerable power peak at the centre of the rod, which causes the clad to split preferentially at this position. The test rods used in the NSRR are much shorter, the active length is typically 125 mm, and the power distribution along the rod is almost uniform. Accordingly, axial splitting of the clad tube is likely to occur along the entire active length of the NSRR test rods.

The NSRR uses stagnant water at atmospheric pressure for cooling. The water is usually at room temperature, but some recent tests have been carried out at somewhat higher temperatures, as shown in table B.2.

The low coolant temperature in the NSRR leads to a more brittle behaviour of the cladding, compared to the conditions in CABRI. Moreover, the coolant in the CABRI reactor consists of liquid sodium at 553 K and 0.5 MPa, which is forced through the test loop by pumps. The density of liquid sodium at this temperature and pressure is similar to that of water, and the same is true for the viscosity. However, an important difference is the boiling point, which is about 1150 K for sodium. The difference in boiling point between sodium and water is likely to affect the post-failure behaviour of the fuel rods, and in particular, the interaction between dispersed fuel fragments and the coolant.

Appendix C: Correlation for fuel solidus temperature

The default model (CABRI2+) for the solidus (melting) temperature in SCANAIR-3.2 was used for determining the onset of fuel pellet melting in our calculations of the core failure limits. As described in (Lamare & Latche, 1995), the solidus temperature is in this model correlated to fuel local burnup and local plutonium content through

$$T_{Sol} = 3113 - 655.3X + 336.4X^2 + 99.9X^3 - \tau\left(3.88 - 6.71X\right). \qquad \text{(C.1)}$$

Here, T_{sol} is the solidus temperature in Kelvin, τ is the fuel local burnup in atomic percent[4], and X is the local plutonium content in terms of atomic fraction

$$X = \frac{\text{atoms Pu}}{\text{atoms Pu} + \text{U}}. \qquad \text{(C.2)}$$

It should be noticed, that both τ and X vary considerably over the pellet radius in high-burnup fuel, as a result of local plutonium production at the pellet periphery. This phenomenon is reflected in the radial variation of fuel solidus temperature across the pellet, as illustrated in figure C.1. The spatial distributions of burnup and plutonium produced within the fuel pellets are calculated with FRAPCON-3.2 for a sequence of time steps in the rod pre-irradiation history. The calculated results for a certain time step are then transferred to SCANAIR-3.2, together with other data that are needed to define burnup dependent fuel rod conditions at beginning of a postulated RIA.

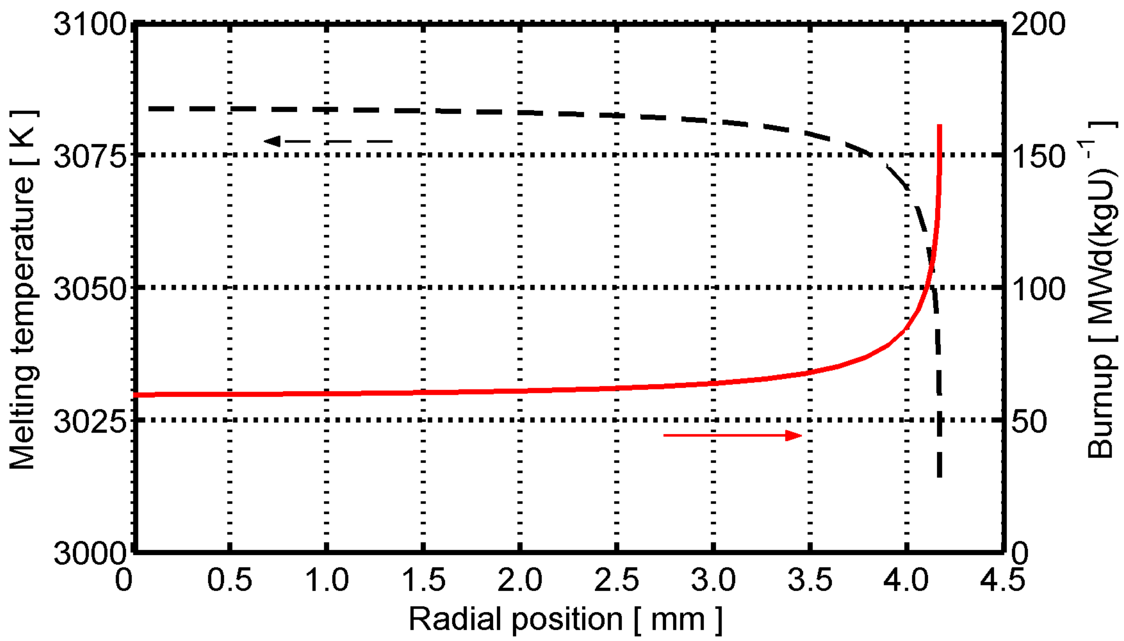

Figure C.1: Calculated variation in fuel melting temperature and burnup across the pellet radius in a typical PWR fuel rod. The pellet radial average burnup is 68 MWd(kgU)$^{-1}$ and the as-fabricated enrichment of ^{235}U is 3.8 % in this example.

[4] A burnup of 1 atomic % corresponds to about 9.38 MWd(kgU)$^{-1}$.

We have not been able to assess the experimental bases to the correlation in eq. (C.1). From the SCANAIR source code and model description (Lamare & Latche, 1995), it is clear that the correlation is based on experimental data produced by the Commissariat á l'Energie Atomique (CEA) in France, which are unavailable to the public.

The correlation in eq. (C.1) is plotted with respect to fuel burnup in figure C.2, assuming $X = 0$. The depression of the solidus temperature with increasing burnup is due to the build-up of fission products in the fuel material. Here, it should be remarked that the depression is substantially less than that predicted by many well-known models, which are based on experimental data from the sixties, e.g. the work of Christensen et al. (1964). These early data are today claimed to be misleading, due to inadequate experimental techniques, see e.g. the work by (Adamson et al., 1985) and the reviews by Fink (1996), Popov et al. (2000) and Carbajo et al. (2001). However, up-to-date experimental data on the melting point of irradiated UO_2 are to our knowledge rare in open literature, which makes it difficult to completely rule out the early works. Most contemporary investigations on nuclear fuel melting are focused on $(U,Pu)O_2$ mixed oxide fuel. In these investigations, melting temperatures are usually measured on a series of irradiated fuel materials with various Pu/U fractions, and the melting temperature of pure UO_2 is derived by extrapolating the results to zero plutonium content. Direct measurements on irradiated UO_2 fuel are rare, but some experimental data of this kind are presented by Komatsu et al. (1988). A model for the burnup dependent melting temperature of UO_2 and $(U,Pu)O_2$ is also given in their work, and this model is shown together with the correlation from SCANAIR in figure C.2. The correlation used in SCANAIR yields a somewhat lower melting temperature than the model by Komatsu and co-workers up to a fuel burnup of 46.5 $MWd(kgU)^{-1}$, whereas the opposite is true for higher burnup. However, the agreement is satisfactory, and in conclusion, the work by Komatsu et al. supports the correctness of the correlation in SCANAIR.

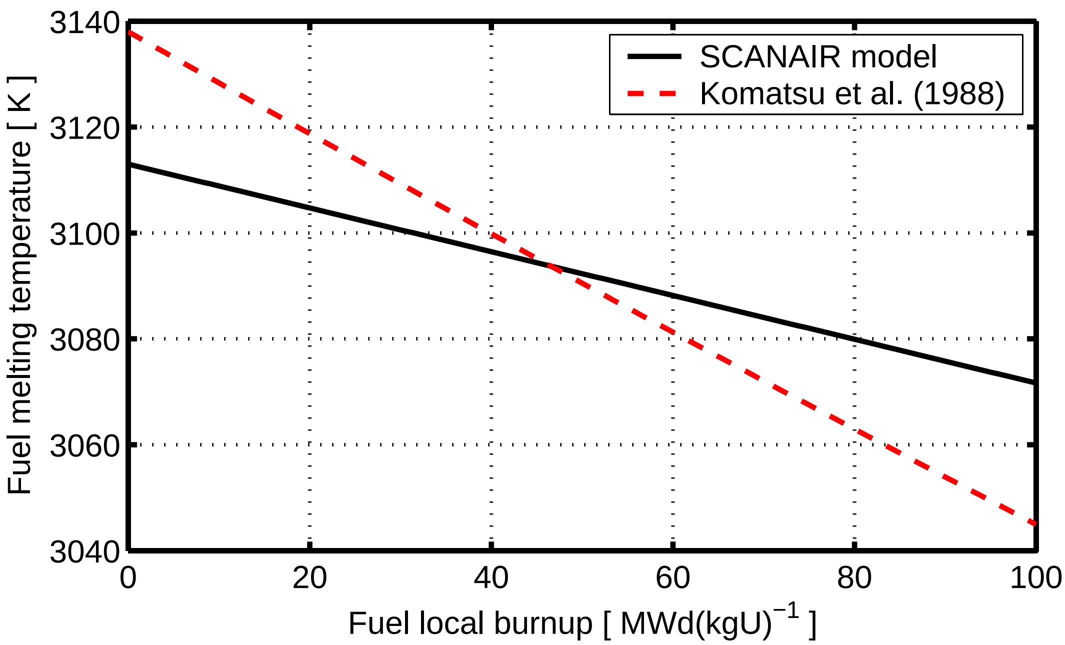

Figure C.2: Calculated solidus (melting) temperature vs. burnup for pure UO_2 fuel.

Appendix D: Correlation for fuel thermal conductivity

The default correlation (HARDING) for thermal conductivity of UO_2 fuel in SCANAIR-3.2 is based on the work of Harding and Martin (1989), and takes the form

$$\lambda \quad = \quad f(P)\left(\frac{1}{g(T,\tau)+3.75\cdot 10^{-2}} \; + \; \frac{4.715\cdot 10^{9}\, e^{-16361/T}}{T^{2}} \right), \qquad \text{(D.1)}$$

where λ is the thermal conductivity [W(mK)$^{-1}$] and T is the fuel temperature [K], see (Lamare, 2001). The porosity correction factor $f(P)$ in eq. (D.1) is taken from the work of Lucuta et al. (1994). It is defined through

$$f(P) \quad = \quad \left(1-P \right)^{2.5}, \qquad \text{(D.2)}$$

where P is the fuel porosity volume fraction [-].

The function g in eq. (D.1) is a correction factor for fuel burnup, defined by

$$g(T,\tau) \quad = \quad 1.55\cdot 10^{-2}\tau \quad + \quad \left(2.165\cdot 10^{-4} - \; 5\cdot 10^{-7}\tau \right)T, \qquad \text{(D.3)}$$

where τ is the local burnup in atomic percent.[5]

The default thermal conductivity correlation in SCANAIR-3.2, given by eqs. (D.1) to (D.3), was slightly modified for the purpose of our analyses. The modification was made, since the above correlation was found to overestimate the thermal conductivity of un-irradiated UO_2, determined in a recent experimental study by Ronchi et al. (1999). In their study, the thermal conductivity of un-irradiated UO_2 was measured with an advanced laser-flash technique. The applied technique was shown to be more precise than conventional laser-flash measurements, especially at high temperatures.

In figure D.1, the thermal conductivity data by Ronchi et al. (1999) are compared with the estimated thermal conductivity of 95 % dense, un-irradiated UO_2, calculated with the above correlation in both original and modified form. As shown in the figure, the correlation was modified, so that a best fit to the data was reached. In the modified correlation, eq. (D.1) was replaced by

$$\lambda \quad = \quad f(P)\left(\frac{0.95}{g(T,\tau)+3.75\cdot 10^{-2}} \; + \; 0.85\,\frac{4.715\cdot 10^{9}\, e^{-16361/T}}{T^{2}} \right). \qquad \text{(D.4)}$$

Hence, the lattice and polaron contribution to the fuel thermal conductivity was reduced by 5 % and 15 %, respectively, with respect to the original correlation in SCANAIR-3.2. The reduced thermal conductivity was used in all calculations of the core failure limits in the present report. The reduced thermal conductivity resulted in calculated enthalpies to fuel melting, which were about 4 cal(gUO_2)$^{-1}$ lower than those calculated with the original correlation for UO_2 thermal conductivity in SCANAIR-3.2.

[5] A burnup of 1 atomic % corresponds to about 9.38 MWd(kgU)$^{-1}$.

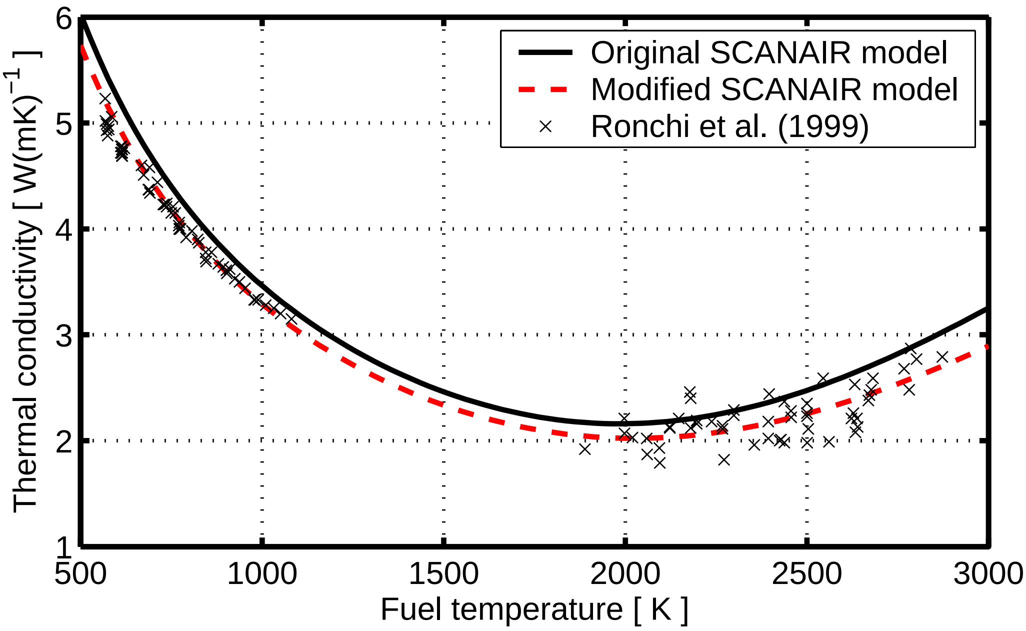

Figure D.1: Calculated thermal conductivity of un-irradiated UO_2, in comparison with the experimental data by Ronchi et al. (1999). The fuel porosity, P, is 0.05 in this particular case.

Appendix E: Power histories and axial power distributions applied in simulations of base irradiation

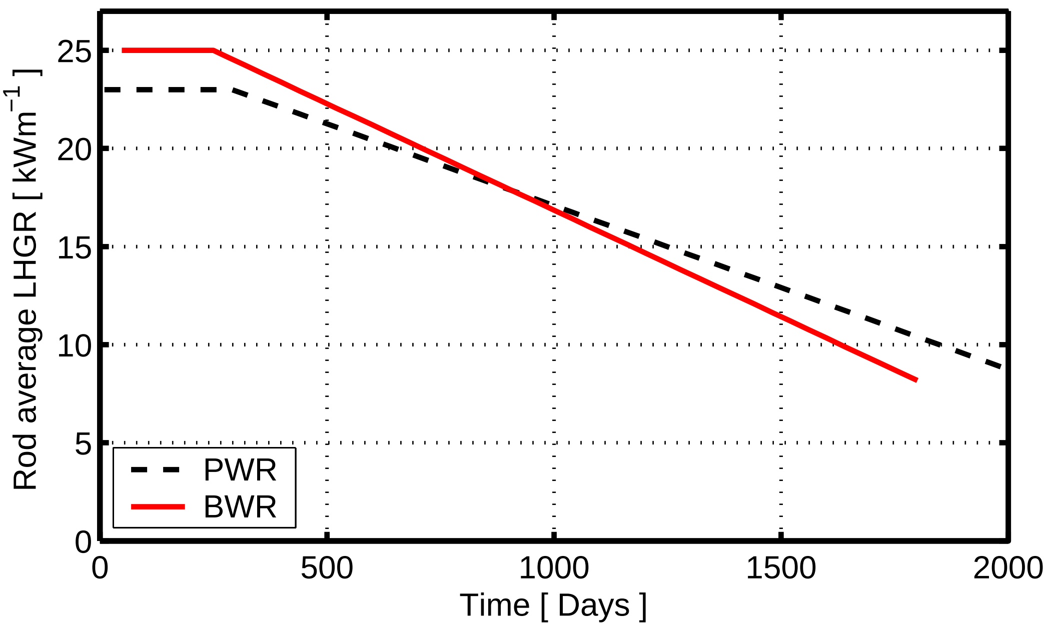

Figure E.1: Fuel rod power histories, applied in simulations of steady-state base irradiation.

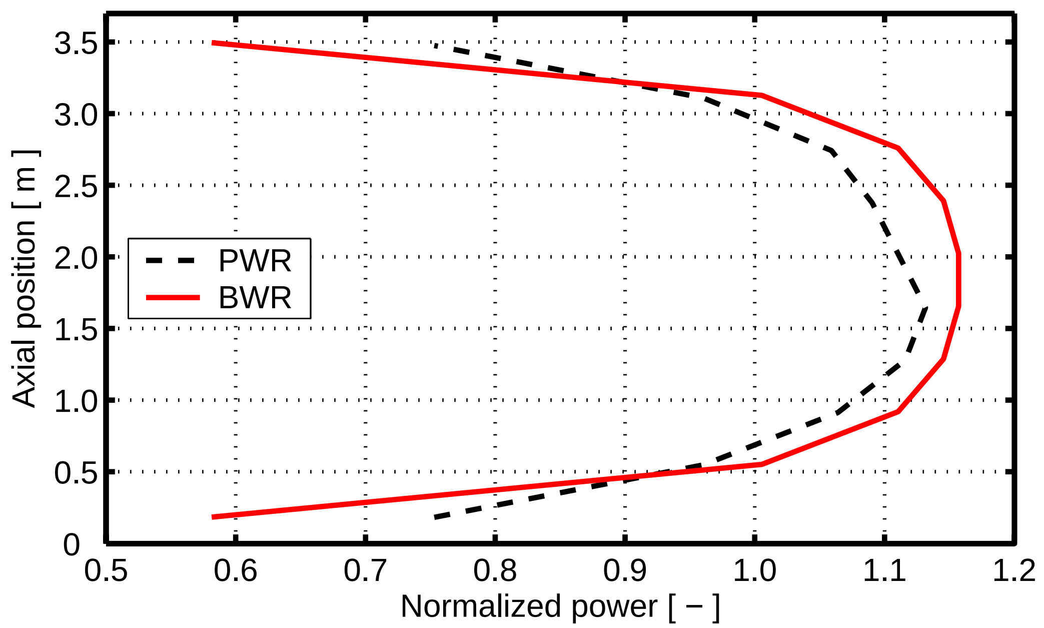

Figure E.2: Fuel rod axial power distributions, applied in simulations of steady-state base irradiation.

Appendix F: Summary of calculated results

Calculated best-estimate conditions under the postulated PWR HZP REA are summarized in table F.1. All data pertain to the rod axial segment at which fuel pellet melting is predicted to occur, i.e. to the axial position of peak power and peak enthalpy. For the PWR fuel rod, this is the 9th axial segment out of 10, corresponding to an axial elevation of 2.9-3.3 m from bottom of the rod.

Likewise, calculated best-estimate conditions under the postulated BWR CZP CRDA are summarized in table F.2. All data pertain to the rod axial segment at which fuel pellet melting is predicted to occur, which for the BWR fuel rod is the 6th axial segment out of 10, corresponding to an axial elevation of 1.8-2.2 m from bottom of the rod. All data in tables F.1 and F.2 are radial average values, except for the peak fuel temperature, which is the peak value with respect to both axial and radial position.

	Fuel pellet burnup [$MWd(kgU)^{-1}$]										
Parameter	25.4	30.3	33.4	37.9	42.1	46.1	51.1	55.6	59.7	64.1	68.0
Peak fuel enthalpy [$J(gUO_2)^{-1}$]	957.1	942.9	934.2	918.8	901.2	884.4	863.9	846.1	832.1	818.5	809.5
Time to peak fuel enthalpy [ms]	101.0	101.0	101.0	101.0	101.0	101.0	101.0	101.0	101.0	101.0	101.0
Fuel enthalpy at fuel melting [$J(gUO_2)^{-1}$]	957.1	942.9	934.2	911.2	893.8	877.2	859.4	841.7	827.7	816.2	807.2
Time to fuel pellet melting [ms]	101.0	101.0	101.0	96.5	96.5	96.5	97.5	97.5	97.5	98.5	98.5
Peak fuel temperature at melting [K]	3096	3093	3091	3087	3085	3083	3080	3078	3075	3073	3071

Table F.1: Calculated fuel enthalpies and temperatures for the PWR HZP REA.

	Fuel pellet burnup [$MWd(kgU)^{-1}$]								
Parameter	29.7	35.3	40.4	45.3	49.8	55.2	60.0	65.2	70.1
Peak fuel enthalpy [$J(gUO_2)^{-1}$]	966.0	951.8	934.8	918.3	902.0	884.1	861.3	839.4	824.5
Time to peak fuel enthalpy [ms]	184.5	184.5	182.5	182.5	182.5	184.5	184.5	184.5	184.5
Fuel enthalpy at fuel melting [$J(gUO_2)^{-1}$]	966.0	945.6	931.7	915.3	899.1	882.6	847.9	830.6	815.7
Time to fuel pellet melting [ms]	184.5	174.5	176.5	176.5	176.5	178.5	170.5	172.5	172.5
Peak fuel temperature at melting [K]	3094	3090	3088	3085	3083	3080	3075	3073	3070

Table F.2: Calculated fuel enthalpies and temperatures for the BWR CZP CRDA.

www.ski.se

STATENS KÄRNKRAFTINSPEKTION
Swedish Nuclear Power Inspectorate

POST/POSTAL ADDRESS SE-106 58 Stockholm
BESÖK/OFFICE Klarabergsviadukten 90
TELEFON/TELEPHONE +46 (0)8 698 84 00
TELEFAX +46 (0)8 661 90 86
E-POST/E-MAIL ski@ski.se
WEBBPLATS/WEB SITE www.ski.se